The Astrophysical Journal, 834:52 (19pp), 2016 January 1 doi:10.3847/1538-4357/834/1/52

THE MEGAMASER COSMOLOGY PROJECT. IX. BLACK HOLE MASSES FOR THREE MASER GALAXIES

F. Gao[1,2,3], J. A. Braatz[2], M. J. Reid[4], J. J. Condon[2], J. E. Greene[5], C. Henkel[6,7], C. M. V. Impellizzeri[2,8], K. Y. Lo[2], C. Y. Kuo[9], D. W. Pesce[10], J. Wagner[6,11], and W. Zhao[1]

[1] Key Laboratory for Research in Galaxies and Cosmology, Shanghai Astronomical Observatory, Chinese Academy of Science, Shanghai 200030, China
[2] National Radio Astronomy Observatory, 520 Edgemont Road, Charlottesville, VA 22903, USA
[3] Graduate School of the Chinese Academy of Sciences, Beijing 100039, China
[4] Harvard-Smithsonian Center for Astrophysics, 60 Garden Street, Cambridge, MA 02138, USA
[5] Department of Astrophysics, Princeton University, Princeton, NJ 08544, USA
[6] Max-Planck-Institut für Radioastronomie, Auf dem Hügel 69, D-53121 Bonn, Germany
[7] King Abdulaziz University, P.O. Box 80203, Jeddah 21589, Saudi Arabia
[8] Joint Alma Office, Alsonso de Cordova 3107, Vitacura, Santiago, Chile
[9] Department of Physics, National Sun Yat-Sen University, No.70, Lianhai Road, Gushan Dist., Kaohsiung City 804, Taiwan (R.O.C.)
[10] Department of Astronomy, University of Virginia, P.O. Box 400325, Charlottesville, VA 22904, USA
[11] Korea Astronomy and Space Science Institute, 776, Daedeokdae-ro, Yuseong-gu, 305-348, Daejeon, Korea
Received 2016 June 22; revised 2016 September 19; accepted 2016 October 20; published 2016 December 29

ABSTRACT

As part of the Megamaser Cosmology Project, we present VLBI maps of nuclear water masers toward five galaxies. The masers originate in sub-parsec circumnuclear disks. For three of the galaxies, we fit Keplerian rotation curves to estimate their supermassive black hole (SMBH) masses, and determine $(2.9 \pm 0.3) \times 10^6\,M_\odot$ for J0437+2456, $(1.7 \pm 0.1) \times 10^7\,M_\odot$ for ESO 558–G009, and $(1.1 \pm 0.2) \times 10^7\,M_\odot$ for NGC 5495. In the other two galaxies, Mrk 1029 and NGC 1320, the geometry and dynamics are more complicated and preclude robust black hole mass estimates. Including our new results, we compiled a list of 15 VLBI-confirmed disk maser galaxies with robust SMBH mass measurements. With this sample, we confirm the empirical relation of $R_{\rm out} \propto 0.3 M_{\rm SMBH}$ reported in Wardle & Yusef-Zadeh. We also find a tentative correlation between maser disk outer radii and *Wide-Field Infrared Survey Explorer* luminosity. We find no correlations of maser disk size with X-ray 2–10 keV luminosity or [O III] luminosity.

Key words: accretion, accretion disks – galaxies: active – quasars: supermassive black holes

Supporting material: machine-readable table

1. INTRODUCTION

The mass of a supermassive black hole (SMBH) is a fundamental parameter of galaxies. Among the dynamical tracers used to measure the SMBH mass directly (e.g., from gas or stars), 22 GHz H_2O megamasers provide the most precise mass estimates outside of our Galaxy. As first demonstrated in the archetypal maser galaxy NGC 4258 (Greenhill et al. 1995; Miyoshi et al. 1995), maser features in such systems trace an edge-on, thin Keplerian disk on sub-parsec scales around the central SMBH and the enclosed mass can be constrained to ±3% (Humphreys et al. 2013). Such disk masers are usually detected in Seyfert 2 galaxies, where the nuclear disk is edge-on and maser emission is beamed into our line-of-sight (LOS).

Over the last two decades, disk maser galaxies have emerged as an important sample for high-precision measurement of SMBH mass, thanks to large surveys (e.g., Braatz et al. 1996, 1997, 2004; Greenhill et al. 2003; Kondratko et al. 2006; Braatz & Gugliucci 2008). In particular, new maser disks are being discovered and mapped by the Megamaser Cosmology Project (MCP, Reid et al. 2009; Braatz et al. 2010)[12], which ultimately aims to use the maser disks to determine the Hubble constant H_0 to better than 3% uncertainty. So far, the MCP has published 7 high-accuracy SMBH masses (Kuo et al. 2011). Including results from other groups (Greenhill & Gwinn 1997, 2003; Herrnstein et al. 1999; Kondratko et al. 2005, 2008; Ishihara et al. 2001; Mamyoda et al. 2009), there are 16 sources measured altogether.

The SMBH mass results can be used to investigate the M–σ relation, as has been done by Greene et al. (2010, 2016). The masses derived from maser galaxies are between $10^6\,M_\odot$ and $10^{7.5}\,M_\odot$ and occupy the less-explored lower-mass end of the M–σ plot. Currently maser galaxies fall below the empirical M–σ relation (e.g., McConnell & Ma 2013). As discussed in Greene et al. (2010) and listed in Kormendy & Ho (2013), many of the host galaxies of maser disks have pseudo-bulges rather than classical bulges, suggesting that galaxies with pseudo-bulges may follow a different M–σ relation than galaxies with classical bulges. As the disk maser sample grows, we could better test whether disk masers are always seen in systems with 10^6 to $10^{7.5}\,M_\odot$ SMBHs and whether maser galaxies with classical bulges follow the empirical M–σ relation.

Some galaxies show maser profiles that differ from the "classical" triple sets of lines characteristic of maser disks. These more complicated systems may harbor outflows (e.g., Circinus; Greenhill et al. 2003; NGC 3079; Kondratko et al. 2005;) and jets (e.g., NGC 1068; Greenhill et al. 1997). Though they are less studied compared to disk masers, as more are imaged, they may become an important sub-sample to study the outflows and interactions of the central active galactic nuclues (AGN) with its environment.

Here we present high-resolution VLBI images and rotation curves of five new maser galaxies: J0437+2456, ESO 558–G009, NGC 5495, Mrk 1029, and NGC 1320. The first three

[12] Project webpage: https://safe.nrao.edu/wiki/bin/view/Main/MegamaserCosmologyProject.

Table 1
Source Information

Source Name (1)	R.A. (J2000) (J2000) (2)	Decl. (J2000) (J2000) (3)	δ R.A. (mas) (4)	δ Decl. (mas) (5)	From (6)	V_{LSR} (km s^{-1}) (7)	δV (km s^{-1}) (8)	AGN Type (9)	Hubble Type (10)
J0437+2456	04:37:03.6840	24:56:06.837	1.3	2	VLBI	4825	40	Sy 2	···
	04:37:03.67	24:56:06.8	500	500	NED				
ESO 558–G009	07:04:21.0113	−21:35:18.948	14	14	VLA-B	7655	27	Sy 2	Sc
Mrk 1029	02:17:03.566	05:17:31.43	500	500	NED	9067	32	Sy 2	···
NGC 5495	14:12:23.35	−27:06 29.20	300	300	VLA-BnA	6741	9	Sy 2	SAB(r)c
NGC 1320	03:24:48.70	−03:02:32.30	300	300	VLA	2649	16	Sy 2	Sa

Note. Positions used for data correlation except for J0437+2456. The position for J0437+2456 (first row) comes from the phase-referenced observation, which has an offset of (191, 36.7) mas (east, north) from the correlation position. The position for NGC 5495 comes from Kondratko et al. (2006).

have spectral profiles indicative of "classical" Keplerian disk masers, while the last two have profiles suggesting more complicated nuclear structure (e.g., Pesce et al. 2015). We note that J0437+2456 and ESO 558–G009 are also current targets for distance measurements with more extensive MCP observations. Here we present preliminary VLBI maps and SMBH masses, based on fitting the rotation curve of high-velocity maser features. We describe our observations and data reduction in Section 2. Section 3 shows the VLBI images and the rotation curves, followed by our analysis of the SMBH masses on each source. Using these results, in Section 4, we define a sample of 15 "clean" disk masers and explore the relation between maser disk radius, SMBH mass and AGN luminosities. Then we give our conclusions in Section 5.

2. OBSERVATIONS

2.1. New Maser Discoveries

We present the first maser maps for five galaxies here. Three of the masers (J0437+2456, ESO 558–G009, Mrk 1029) were discovered in 2010 by our MCP survey. This survey covers Sy 2 galaxies identified from the Sloan Digital Sky Survey (SDSS), Sy 1.8–2.0 from NASA/IPAC Extragalactic Database (NED), and Sy 2 galaxies identified from the Two Micron Redshift Survey. All survey observations were conducted using the Robert C. Byrd Green Bank Telescope (GBT).[13] The survey will be described fully in a forthcoming paper (J. A. Braatz et al. 2016, in preparation).

The maser in NGC 5495 was discovered by Kondratko et al. (2006) during a survey of Sy 1.8–2.0 and LINER galaxies with $v_{sys} \leqslant 14{,}000$ km s^{-1} using the NASA DSN antennas, and the maser in NGC 1320 was discovered by Greenhill et al. (2009) in a survey of galaxies with inclined stellar disks with the GBT.

All of these galaxies are Sy 2 AGN, with recession velocities between 2663 and 9076 km s^{-1}. Their host galaxies are all late-type galaxies. We list their host galaxy properties in Table 1. Figure 1 shows a GBT single-dish spectrum for each source observed closest to the VLBI observing dates (with a maximum time separation of 60 days). For NGC 1320, we show the GBT spectra observed before and after the VLBI observation in Figure 1, showing significant variability. The original spectral resolution of the GBT spectra was 24.4 kHz (≈0.3 km s^{-1}). However, for comparison with the VLBI results, these spectra were smoothed to the same spectral resolution as the VLBI observations.

[13] The Green Bank Telescope is a facility of the National Radio Astronomy Observatory.

2.2. VLBI Observations

The VLBI observations were conducted between 2010 and 2014 using the Very Long Baseline Array (VLBA)[14] together with the GBT, and in some cases also with the Effelsberg 100 m telescope (EB) and the phased Karl G. Jansky Very Large Array (VLA). We list the basic VLBI observing information in Table 2, including the experiment code, date observed, track duration, antennas used, beam size, sensitivity, and the observing strategy. All but one (J0437+2456) of the galaxies were observed with similar setups as described below.

For ESO 558–G009, Mrk 1029, NGC 5495 and NGC 1320, we conducted the observations using a "self-calibration" strategy, in which we remove atmospheric phase fluctuations using a strong, narrow maser line from the target maser galaxy. Two "geodetic blocks," bracketing the maser observations were used to calibrate the tropospheric delay and clock errors at each antenna. The geodetic blocks were generated by SCHED automatically, with each block lasting about 45 minutes. For the details of geodetic block setup and data reduction, please refer to Mioduszewski & Kogan (2000) and Reid et al. (2009). For the maser observations, we observed four IF pairs in dual polarization, with a bandwidth of 16 MHz in each IF. Three IF pairs were set to cover the systemic, the blueshifted and the redshifted masers, respectively, with the fourth covering any additional emission seen in the single-dish spectrum. The spectral coverage in our VLBI observations is shown in Figure 1 as the horizontal solid lines below the GBT spectra. We observed a nearby delay calibrator about every 50 minutes to calibrate the single band delay, and a bandpass/fringe-finder source was observed twice in each track. Our data were recorded with the Mark 5B recording system (a.k.a. the VLBA legacy system) with the maximum recording rate of 512 Mbit s^{-1} and maximum bandwidth of each baseband limited to 16 MHz.

For "self-calibration" observations, to map the maser distribution optimally and derive the best SMBH mass, an accurate absolute position of the reference feature is needed. A large offset between the true absolute position and the position used in VLBI correlation will introduce a significant phase error that varies with observed frequency, contributing an additional positional uncertainty for each maser spot, distorting our final map and affecting the measured warping in the position angle (P.A.) direction (Gao et al. 2016). Typically an

[14] The VLBA is a facility of the National Radio Astronomy Observatory, which is operated by the Associated Universities, Inc. under a cooperative agreement with the National Science Foundation (NSF).

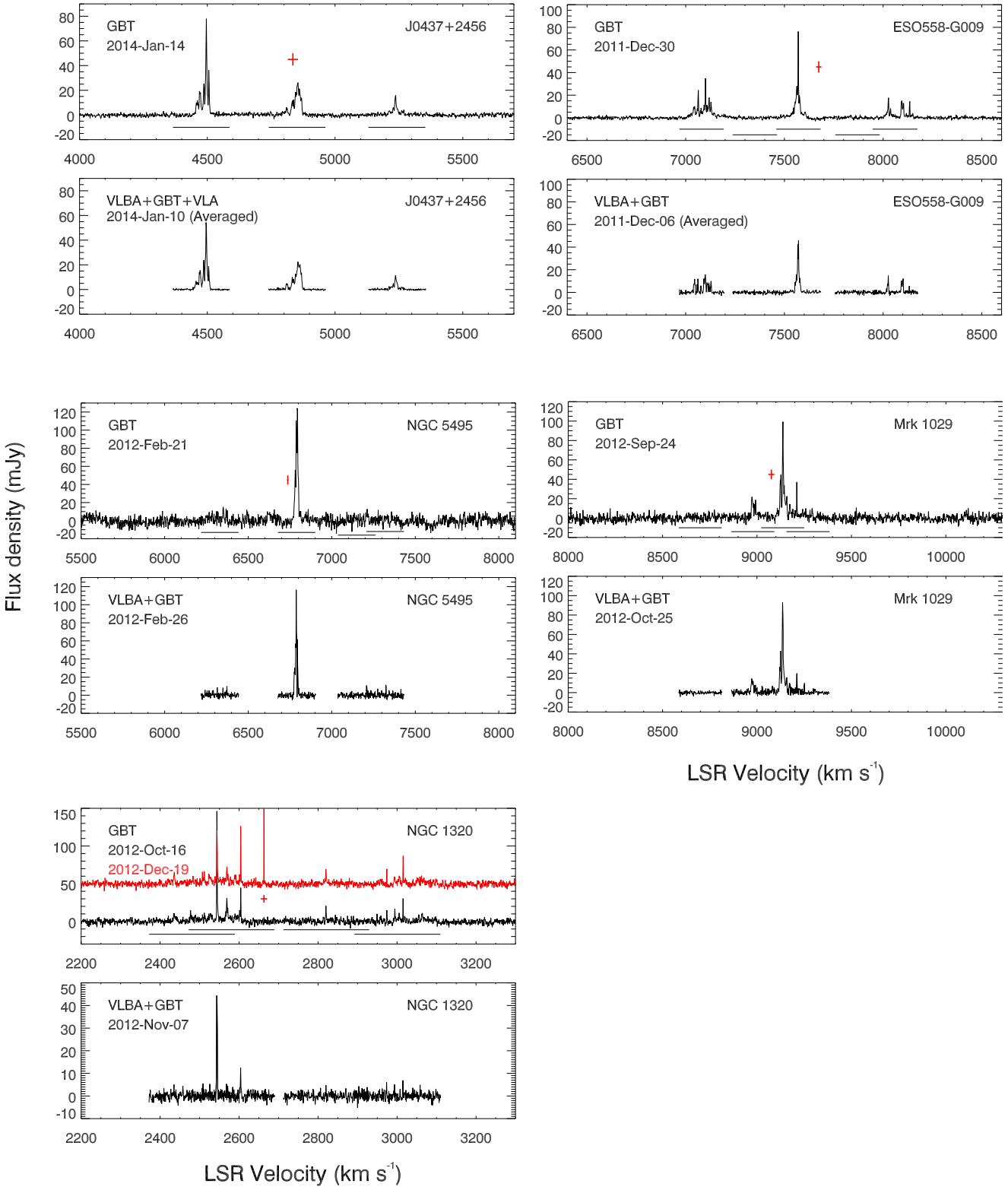

Figure 1. A GBT single-dish spectrum and the VLBI spectrum for each of the five targets. For each galaxy, the single-dish spectrum is shown in the upper panel. Except for NGC 1320, we use the same scale for intensity when comparing the two spectra. The single-dish spectrum is smoothed to have the same channel size as the VLBI spectrum, except for ESO 558–G009, in which the VLBI spectral resolution for the systemic part is ≈3.55 km s^{-1}, while the spectral resolution in the single-dish spectrum is 1.8 km s^{-1}. The mismatched channels cause the apparent difference in intensity of the systemic features between the single-dish spectrum and the VLBI spectrum. The red crosses indicate the recession velocity of the galaxy reported from NED, with the horizontal bar indicating the uncertainty. The black solid horizontal lines beneath the spectra indicate the velocity coverage in our VLBI imaging observations. For J0437+2456, the solid lines show the zoom-band we used for the final correlation pass. The original dual 128 MHz bands cover the full velocity extent for J0437+2456 as shown here.

Table 2
VLBI Observation Details

Project Code	Date Observed	Source Name	Antennas Used	Beam Size (mas × mas, deg)	Track Length (hour)	Sensitivity	Observing Strategy
(1)	(2)	(3)	(4)	(5)	(6)	(7)	(8)
BB278 K	2010 Nov 22	J0437+2456	VLBA+GB+EB	0.90 × 0.27, −17	12	1.10	Phase-ref.
BB278 L	2010 Nov 28	J0437+2456	VLBA+GB+EB	0.69 × 0.23, −13	12	0.62	Self-cal.
BB321 X0	2014 Jan 03	J0437+2456	VLBA+GB+VLA	1.28 × 0.50, −14	6	0.70	Self-cal.
BB321 X1	2014 Jan 04	J0437+2456	VLBA+GB+VLA	0.98 × 0.38, −16	6	0.60	Self-cal.
BB321 X4	2014 Jan 24	J0437+2456	VLBA+GB+EB+VLA	1.11 × 0.32, −15	6	0.50	Self-cal.
X0+X1+X4		J0437+2456		1.11 × 0.37, −15	···	0.34	Self-cal.
BB278 T	2011 Nov 01	ESO 558–G009	VLBA+GB	1.30 × 0.34, −10	8	1.65	Self-cal.
BB278 X	2012 Jan 11	ESO 558–G009	VLBA+GB	1.39 × 0.46, −2	8	1.33	Self-cal.
BB313AF	2012 Nov 18	ESO 558–G009	VLBA+GB	1.30 × 0.41, −9	8	···	Phase-ref.
T+X		ESO 558–G009		1.30 × 0.39, −6	···	1.10	Self-cal.
BB313 C	2012 Feb 26	NGC 5495	VLBA+GB	1.49 × 0.38, −11	6	2.10	Self-cal.
BB313 AA	2012 Oct 25	MRK 1029	VLBA+GB	1.14 × 0.49, −3	10	1.40	Self-cal.
BB313 AB	2012 Nov 07	NGC 1320	VLBA+GB	1.20 × 0.39, −8	9	1.46	Self-cal.

Note. Sensitivity listed in Column 7 is in the unit of mJy Beam^{-1} Chan^{-1}. BB278K did not include BR, and BB278X did not include MK. The track length includes two geodetic blocks of 1.5 hr in total. Because of the low declination, the track lengths for ESO 558–G009 and NGC 5495 are just 8 and 6 hr, respectively. The channel sizes used in the final VLBI maps are 100 kHz (J0437+2456), 125 kHz (ESO558–G009, NGC 5495, MRK 1029), and 62.5 kHz (NGC 1320).

absolute position accuracy of ≈10 mas is sufficient in our MCP observations. Otherwise the systematic errors resulting from this effect should also be considered (see Section 3.3 for more details).

We conducted a phase-referenced VLBI observation of J0437+2456 to measure the absolute position of the maser. We observed an external calibrator J0435+2532 (0.°70 away) every 70 s to remove the atmospheric phase variations. We followed the data reduction process for phase-referencing observations as described in Reid et al. (2009). Finally we derived the sky position of the peak maser emission at velocity 4495.38 km s^{-1}, to be at R.A. = $04^{h}37^{m}03.^{s}6840$ and decl. = $+24°56'06.''837$, with uncertainties of 1.3 mas and 2 mas respectively. We used this position for data correlation in the subsequent "self-cal" tracks.

For ESO 558–G009, we used the VLA in B configuration to measure the maser position R.A. = $07^{h}04^{m}21.^{s}011$ and decl. = $-21°35'19.''948$ with uncertainties of 33 mas and 64 mas, respectively, prior to our VLBI observations. To better constrain the maser position, we conducted a phase-referenced VLBI observation (BB313AF) in which an external calibrator J0702–1951 (1.°77 away) was observed every other minute. However, due to the relative weakness of the peak maser line intensity (<40 mJy, measured from the GBT single-dish spectrum taken within one month to the VLBI observation), and phase de-coherence in the phase transfer from J0702–1951 to ESO 558–G009, we were unable to detect the signal from ESO 558–G009. So we applied the VLA position of ESO 558–G009 for VLBI correlation.

Because of the relatively low intensity of maser lines in J0437+2456 (with peak intensity usually less than 50 mJy), the majority of "self-cal" tracks for J0437+2456 were conducted between 2013 and 2014 (with three tracks presented here), when we could include the phased-VLA in our observation array, boosting our sensitivity by ≈40%. During observations, we "phased-up" all of the VLA antennas prior to each VLBI scan. This was done by observing J0435+2532 (>140 mJy, 0.°7 away from J0437+2456) for 1 minute. To minimize decorrelation, we set the maximum VLBI scan length to be 10 minutes with the VLA in B- or C-configuration. We also added a flux calibration scan for the VLA to get the combined system temperature for the phased array. We used the Mark 5C recording system, which offers a maximum recording rate of 2 Gbit s^{-1}, enabling us to cover the entire maser spectrum with two 128 MHz bands (≈1700 km s^{-1} for each band) in dual polarization and 2-bit sampling. In order to obtain high spectral resolution for the maser data, we re-correlated 16 MHz portions of these broad bands with the new zoom-bandmode offered in the DiFX software correlator (Deller et al. 2007). Figure 1 shows the velocity coverage of the zoom-bands for J0437+2456 as horizontal dashed lines below the GBT spectrum. For comparison, the original dual 128 MHz bands cover the full velocity range shown in Figure 1. For each of the self-calibrated tracks, we did not observe geodetic blocks, since we used the hourly delay calibrator observations to solve for and remove residual multi-band delays.

All data were calibrated using the NRAO Astronomical Image Processing System (AIPS). For the self-calibration tracks, we followed the data reduction process described in Reid et al. (2009). The typical solution interval used in CALIB varied between 1 and 2 minutes, depending on the coherence times in each track.

For J0437+2456, before the final imaging step, we averaged the (u, v) data to 1.4 km s^{-1} per channel (100 kHz) to match the typical spectral linewidths from the single-dish spectrum. After we made images for tracks BB321X0, BB321X1 and BB321X4 separately, we combined the data before imaging, assuming that the strongest feature at 4496.15 km s^{-1} did not change its position. Since we observed the tracks within a month, this is a safe assumption.

For ESO 558–G009, we averaged the interferometer spectra to 3.55 km s^{-1} per channel (250 kHz) for the systemic features, and 1.8 km s^{-1} per channel (125 kHz) for the high-velocity features. Then we calibrated the data from tracks BB278X and BB278T separately and combined them in the (u, v) domain by aligning the strongest systemic feature at velocity 7572 km s^{-1}. Then we made images from the combined data.

For Mrk 1029 and NGC 5495, we averaged the (u, v) data to 1.8 km s^{-1} per channel (125 kHz). For NGC 1320, no averaging was performed on the (u, v) data. The raw data

Table 3
Sample Data for J0437+2456

Velocity (km s^{-1}) (1)	R.A. (mas) (2)	δR.A. (mas) (3)	Decl. (mas) (4)	δdecl. (mas) (5)	Surface Brightness (mJy Beam^{-1} Chan^{-1}) (6)	Noise (mJy Beam^{-1} Chan^{-1}) (7)
J0437+2456						
4872.99	0.0537	0.01535	0.0527	0.03773	4.49	0.34
4871.59	0.0213	0.01034	0.0337	0.02288	6.94	0.34
4870.20	0.0150	0.00539	0.0470	0.01243	13.07	0.34
4868.81	0.0091	0.00515	0.0623	0.01202	13.54	0.34
4867.41	0.0365	0.00564	0.0165	0.01324	11.91	0.34

(This table is available in its entirety in machine-readable form.)

has spectral resolution of 0.86 km s^{-1} per channel (62.5 kHz). We list the beam size and 1σ image sensitivity for each track in Table 2. The VLBI-imaged maser components for each galaxy are listed in Table 3.

3. BLACK HOLE MASS FITTING AND RESULTS

3.1. Fitting Method

The SMBH mass from a disk maser galaxy can be determined using the rotation curve measured from high-velocity maser features in a VLBI map (e.g., Kuo et al. 2011). The model can be generalized to 3D if spectral monitoring observations are made to measure the LOS accelerations of individual maser features, which are essential to derive the physical radius of the systemic maser features and thus determine the geometric distance to the maser disk (e.g., Humphreys et al. 2013; Reid et al. 2013; Gao et al. 2016). Among the five galaxies presented here, J0437+2456 and ESO558–G009 were observed with the GBT to monitor the spectral features. Analysis of these observations is ongoing, so in this paper we utilize only the rotation curve from high-velocity features to estimate the SMBH masses for all five galaxies. A full 3D analysis of the maser disk in J0437+2456 and ESO 558–G009 will be present in subsequent work.

Our estimation of the SMBH mass depends directly on the distance to the host galaxy. In this paper, we derive the galaxy distances based on their recession velocity with an H_0 of 73 km s^{-1} Mpc^{-1}, in concordance with the previous MCP work by Kuo et al. (2011). We present all the VLBI images together with the position–velocity (P–V) diagrams and residuals in Figures 2 and 3. We determine the black hole mass by applying the following steps.

First we defined the position angle of the disk with respect to the redshifted masers, from due north to the east. According to such a position angle, we rotate the VLBI image with respect to a reference feature so that the major axis of the maser disk lies horizontally. Then we minimize the vertical offsets of the high-velocity features by shifting all the data vertically. We estimate the disk inclination angle as $\cos^{-1} i = \bar{\theta_y}/\bar{\theta_r}$, following the same treatment in Kuo et al. (2011), in which $\bar{\theta_y}$ is the averaged vertical offset of the systemic masers from the disk plane defined by the high-velocity masers, $\bar{\theta_r}$ is the averaged angular separation between the systemic masers and the high-velocity masers, which we equate to the radius of the high-velocity features. Here we have assumed all the systemic masers are located on the same radius as the high-velocity masers. Then we define the impact parameter in the P–V diagram as the radial offset $r_i = [(x_i - x_0)^2 + (y_i - y_0)^2]^{\frac{1}{2}}$ of each maser spot from the reference feature (x_0, y_0). Here, x_i and y_i represent maser positions after the coordinate rotation and vertical displacement. Features on the redshifted side have positive values of the impact parameter, while features on the blueshifted side have negative values. The reference feature is usually the one with a velocity closest to the reported recession velocity. If all the systemic features are offset from the reported recession velocity, then we use the strongest systemic feature as the reference, as in the case of ESO 558–G009.

We fit the rotation curve of the high-velocity features with a Keplerian rotation model, in which

$$v_{\mathrm{rot}_i} = \left[\frac{GM}{(r_i - r_0)}\right]^{\frac{1}{2}}. \quad (1)$$

Here $v_{\mathrm{rot_i}}$ is the Keplerian rotation speed of the ith maser feature around a central black hole with mass M. The reference position r_0 refers to the dynamical center on the maser disk plane, and r_i is the impact parameter of the ith maser feature with respect to this reference position. The observed recession velocity is related to the Keplerian rotation velocity by the following:

$$v_{\mathrm{LSR,opt}} = v_{\mathrm{rot}_i} \sin i + v_0 + v_{\mathrm{rel_i}} \quad (2)$$

where

$$v_{\mathrm{rel_i}} \simeq \frac{1}{2c}[(v_{\mathrm{rot}_i} + v_0)^2 + v_{\mathrm{rot}_i}^2 \cos^2 i + 2v_{\mathrm{rot}_i}^2]. \quad (3)$$

Here $v_{\mathrm{rel_i}}$ is the velocity correction for both the special and general relativistic effects for the ith maser feature (Herrnstein et al. 2005), and v_0 is the systemic velocity of the galaxy, defined in the relativistic frame. $v_{\mathrm{LSR,opt}}$ is the LSR velocity of each observed maser feature, using the optical definition of velocity. i is the inclination angle of the maser disk derived above, with 90° corresponding to edge on. Here we assume all the high-velocity features are located on the mid-line of the disk, where the mid-line is defined as the diameter through the disk perpendicular to the LOS.

A Bayesian method was used in our fitting to get the best-fit M, r_0, and v_0. We use the Markov Chain Monte-Carlo approach to sample the parameter space and the Metropolis–Hastings algorithm to explore the probability density function (PDF) for each parameter, in which we aimed at 25% acceptance rate.

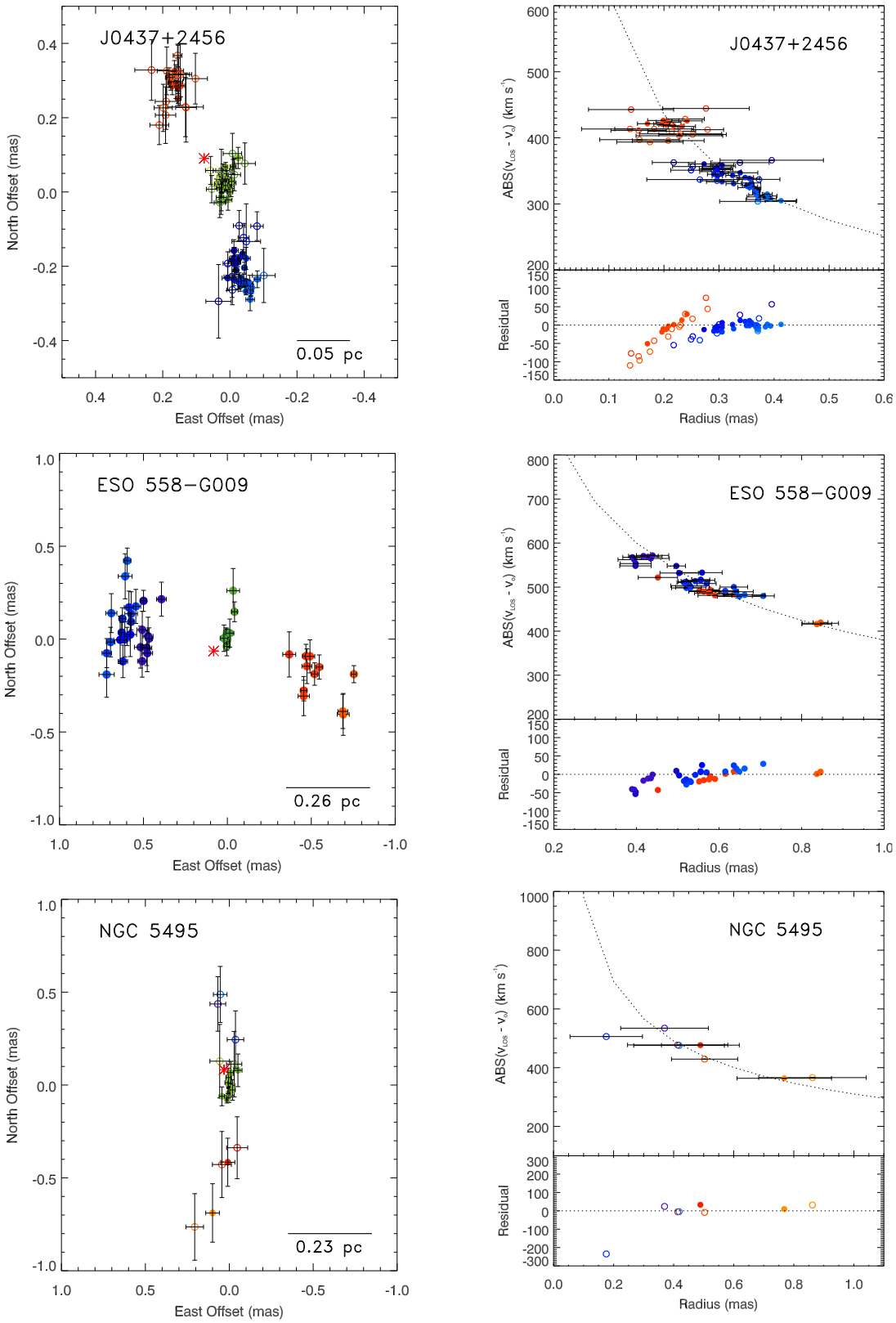

Figure 2. The VLBI maps with *P*–*V* diagrams for the 3 disk masers: J0437+2456, ESO 558–G009 and NGC 5495. Residuals are shown on the bottom of the *P*–*V* diagram. For J0437+2456 and ESO 558–G009, maser spots with intensity above 5σ are shown here, and we highlight maser features brighter than 5 mJy in filled circles in J0437+2456. For NGC 5495, features between 3σ and 5σ are shown in open circles. The red asterisk marks the fitted dynamical center on the VLBI map. The dotted line on the *P*–*V* diagram shows the best-fit Keplerian rotation curve. Maser spots on the *P*–*V* diagram are referenced to the fitted dynamical center on the *X*-axis.

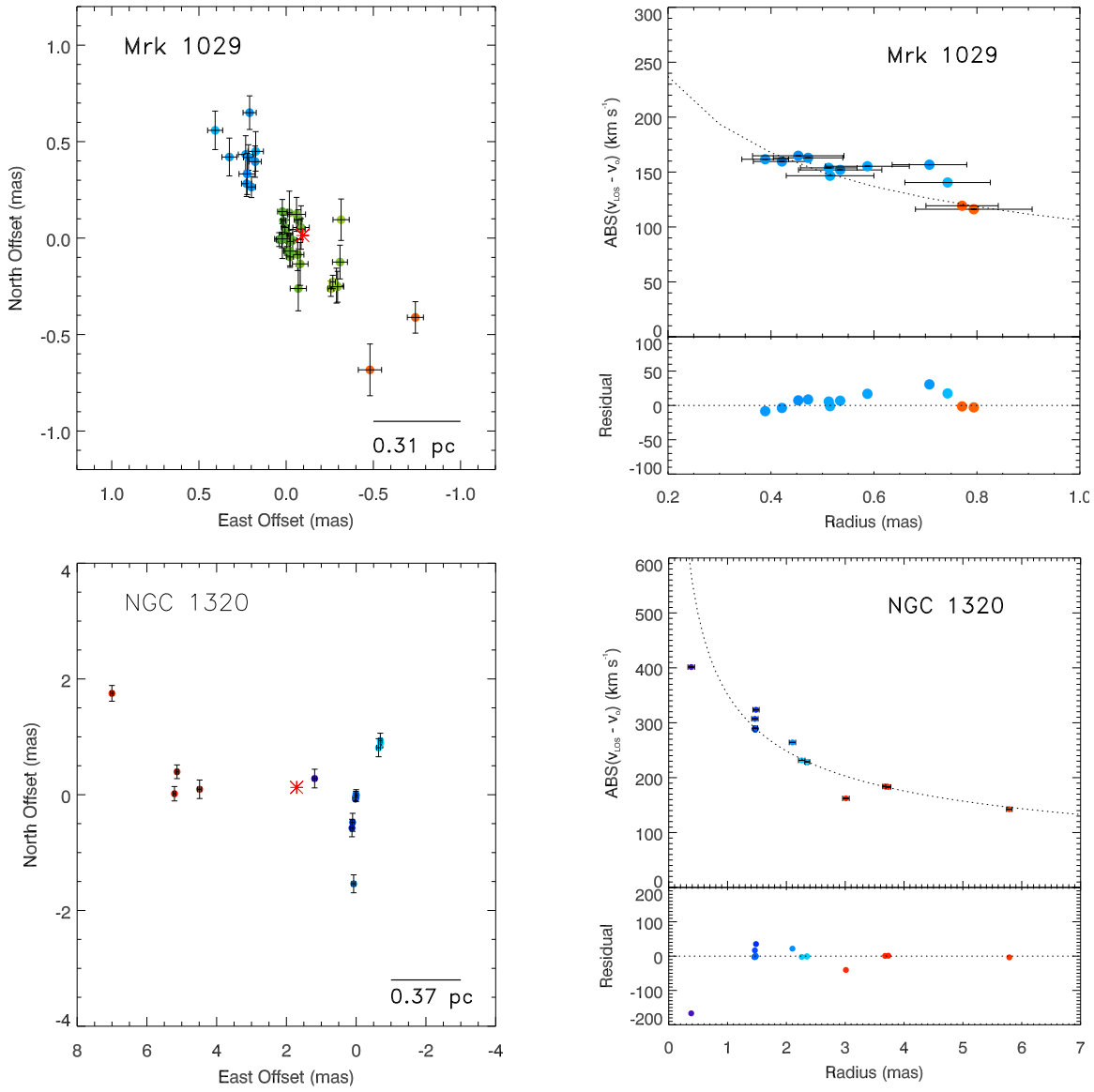

Figure 3. The VLBI maps and *P–V* diagrams for Mrk 1029 and NGC 1320, which are not typical Keplerian disk maser systems but do show a configuration consistent with circumnuclear rotation. Residuals are shown on the bottom of the *P–V* diagram. All features shown here are above 5σ.

The χ^2 of the model fit is given by

$$\chi^2 = \sum_i \frac{(v_{\mathrm{LSR,opt},i} - v_{\mathrm{rot}_i} - v_0 - v_{\mathrm{rel}_i})^2}{\sigma_{v,i}^2}. \quad (4)$$

Here the velocity uncertainties $\sigma_{v,i}$ are expressed by the uncertainties in the measured position of masers:

$$\sigma_{v,i}^2 = \frac{1}{4} v_{\mathrm{rot}_i}^2 \frac{(x_i - x_0)^2 \sigma_{x,i}^2 + (y_i - y_0)^2 \sigma_{y,i}^2}{[(x_i - x_0)^2 + (y_i - y_0)^2]^2} \quad (5)$$

where $\sigma_{x,i}$ and $\sigma_{y,i}$ are the measured VLBI positional uncertainties projected along and perpendicular to the maser disk plane after the coordinate rotation. Note that values of y_0 are fixed to zero in the actual fitting since we place the dynamical center on the maser disk plane, and assume the maser disk is flat with all high-velocity features on the mid-line of the disk. As shown in Equation (2), there is a degeneracy between the inclination angle and the rotation velocity. Adding the inclination angle as another free parameter in the fitting will dramatically slow down the fitting convergence, so we did not fit the inclination angle here.

We use flat prior for the three fitting parameters, unless otherwise stated. Typically, we discarded 10^7 burn-in trials before generating 9×10^7 trials for parameter estimation. We binned these 9×10^7 trials to generate the final PDF. For each parameter, we quote the mode in the final PDF as the fitted value, and sum up the final PDF to find the $\pm 34\%$ from the mode as the 1σ uncertainty. All uncertainties have been scaled by $\sqrt{\chi^2/N}$. Below we describe the VLBI and black hole mass fitting results for each galaxy individually, and in Section 3.2 we list several sources of systematic errors in the fitting process. We note that the SMBH mass uncertainties reported in Section 3.2 do not include the uncertainty in H_0, but they are added later as part of the systematics.

Table 4
The SMBH Masses and Basic Properties of the Maser Galaxies

Name	Dist. (Mpc)	SMBH Mass ($M_\odot$)	Fitted Recession Velocity (km s^{-1})	R_{in} (pc)	R_{out} (pc)	P.A. (°)	Incl. (°)
(1)	(2)	(3)	(4)	(5)	(6)	(7)	(8)
J0437+2456	65.3 ± 3.6	2.9 ± 0.3 × 10^6	4807.6 ± 10.5	0.04 ± 0.03	0.13 ± 0.03	20 ± 2	81 ± 1
ESO 558–G009	107.6 ± 5.9	1.7 ± 0.1 × 10^7	7599.0 ± 14.0	0.20 ± 0.05	0.47 ± 0.06	256 ± 2	98 ± 1
NGC 5495	95.7 ± 5.3	1.1 ± 0.2 × 10^7	6839.6 ± 67.0	0.10 ± 0.05	0.30 ± 0.05	176 ± 5	95 ± 1
Mrk 1029*	120.8 ± 6.6	1.9 ± 0.5 × 10^6	9129.9 ± 26.0	0.23 ± 0.12	0.45 ± 0.12	218 ± 10	79 ± 2
NGC 1320*	34.2 ± 1.9	5.5 ± 2.5 × 10^6	2829.2 ± 11.4	⋯	⋯	90 ± 10	90*

Note. Column (1): Galaxy name. Column (2): Distance, taken from NED using the Hubble flow with an H_0 of 73 km s^{-1} Mpc^{-1}. Column (3): The fitted SMBH mass. Column (4): Fitted recession velocity from VLBI. Columns (5–6): The inner and outer radius of the maser disk, estimated from the high-velocity maser features. Please refer to Section 4.2 for a more comprehensive analysis. Column (7): Position angle of the disk. Column (8): Inclination angle of the disk. We note that since the maser configuration in Mrk 1029 and NGC 1320 are not typical for a disk maser, their fitted SMBH mass, recession velocity, disk size, and position angle listed here are just indicative under a thin disk model. And we cannot estimate the disk inclination angle for NGC 1320 due to the lack of systemic masers, so we fixed it to 90°.

3.2. Notes on Individual Sources

3.2.1. J0437+2456

The VLBI map of J0437+2456 shown in Figure 2 has a flux cutoff of 1.7 mJy beam^{-1} channel^{-1} (with a channel width of 100 kHz), which is at the 5σ level. We highlight features above 5 mJy in filled circles. The VLBI map shows an edge-on disk in a linear configuration, with a P.A. of 20° ± 2°. There is a slight misalignment between the systemic masers and the high-velocity masers. The estimated inclination angle of the disk is 81° ± 1°.

The best-fit (with reduced χ^2 of 1.07) black hole mass is (2.9 ± 0.1) × 10^6 $M_\odot$, with recession velocity $V_0^{\rm LSR,opt}$ of 4809.5 ± 10.5 km s^{-1}. The dynamical center is located + 0.12 mas from the original reference position (with velocity of 4835 km s^{-1}) on the major axis of the maser disk. The inner and outer radius of the disk are about 0.11 and 0.42 mas, which corresponds to 0.035 and 0.13 pc. The uncertainty on the SMBH mass is ±3.4%. We note that on the *P–V* diagram, the redshifted features are scattered horizontally with a positive slope on the residual plot, in contrast to the well-fit blueshifted features. The pattern in the residuals may be influenced by unmodeled disk structure, with the model fit limited by low signal-to-noise. Higher-sensitivity VLBI observations and 3D modeling of the maser disk should resolve the full disk structure. Nevertheless, since it is the blueshifted masers that mostly constrain the SMBH mass result here (with higher S/N, larger velocity coverage), our best-fit SMBH mass is still robust. We show the PDF for the dynamical center position, the SMBH mass and the recession velocity in Figure 4.

From single-dish monitoring observations aimed at measuring the accelerations of the systemic features, and unrelated to the SMBH mass measurement we present here, we found the strongest features in J0437+2456 increased in flux from 45 mJy (2013 December 19) to 85 mJy (2014 January 14) then fell back to 40 mJy (2014 February 19). By catching such maser brightening in our VLBI observations (BB321X0, BB321X1 and BB321X4), we were able to calibrate the interferometer phase on the strongest maser line. Even when including the VLA, it is difficult to solve for the fringe phase from a spectral line feature less than 50 mJy, with a channel size of 1.4 km s^{-1} and a solution interval of 1–2 minutes.

3.2.2. ESO 558–G009

The 1σ noise of the ESO 558–G009 VLBI map is about 1.1 mJy beam^{-1} channel^{-1}, using a channel width of 125 kHz. We plot all the maser features brighter than 5.5 mJy in Figure 2. The map shows an edge-on maser disk at a P.A. of 256° ± 2°. Because of the low declination of ESO 558–G009 (−21°), the synthesized beam is elongated in the north–south direction, approximately perpendicular to the disk, so the map does not tightly constrain the disk thickness. The vertical offset of the major axis of the maser disk is −0.082 mas. We estimate the inclination angle of the disk to be 98° ± 1°.

The high-velocity masers in ESO 558–G009 are well fitted with a Keplerian rotation curve, as shown in Figure 2. The best-fit (with reduced χ^2 of 1.28) black hole mass is (1.70 ± 0.02) × 10^7 $M_\odot$ and the recession velocity $V_0^{\rm LSR,opt}$ is 7595.9 ± 14.0 km s^{-1}. The dynamical center is located −0.064 mas from the original reference position (with velocity of 7591 km s^{-1}) on the major axis of the maser disk. The inner and outer radius of the disk are about 0.38 and 0.9 mas, corresponding to 0.20 and 0.47 pc. The uncertainty on the SMBH mass is ±1.5%. We show the PDF for the dynamical center position, the SMBH mass and the recession velocity in Figure 4.

3.2.3. NGC 5495

The VLBI map of NGC 5495 shown in Figure 2 uses a 3σ flux cutoff of 6.3 mJy beam^{-1} channel^{-1} with a channel width of 125 kHz, in contrast to the 5σ flux cutoff we normally used here. This is because there will be no blueshifted features left when we apply a 5σ cutoff and thus we cannot constrain the SMBH mass accordingly. So here we lowered our criteria to have the fitting run successfully. The VLBI image shows a north–south orientation of the maser disk, with a P.A. of 176° ± 5°. We estimate the inclination angle of the disk to be 95° ± 1°. The inner and outer radii of the disk are about 0.22 and 0.65 mas, corresponding to 0.10 and 0.30 pc. The high-velocity features show evidence for strong warping in the P.A. direction on the redshifted side. Features with intensity above 5σ are shown in filled circles on the VLBI map, while those in between 3σ and 5σ are shown in open circles.

Our best-fit (with reduced χ^2 of 0.22) SMBH mass for NGC 5495 is (1.05 ± 0.06) × 10^7 $M_\odot$. The fitted recession velocity $V_0^{\rm LSR,opt}$ is 6839.6 ± 67.0 km s^{-1}. The uncertainty on the

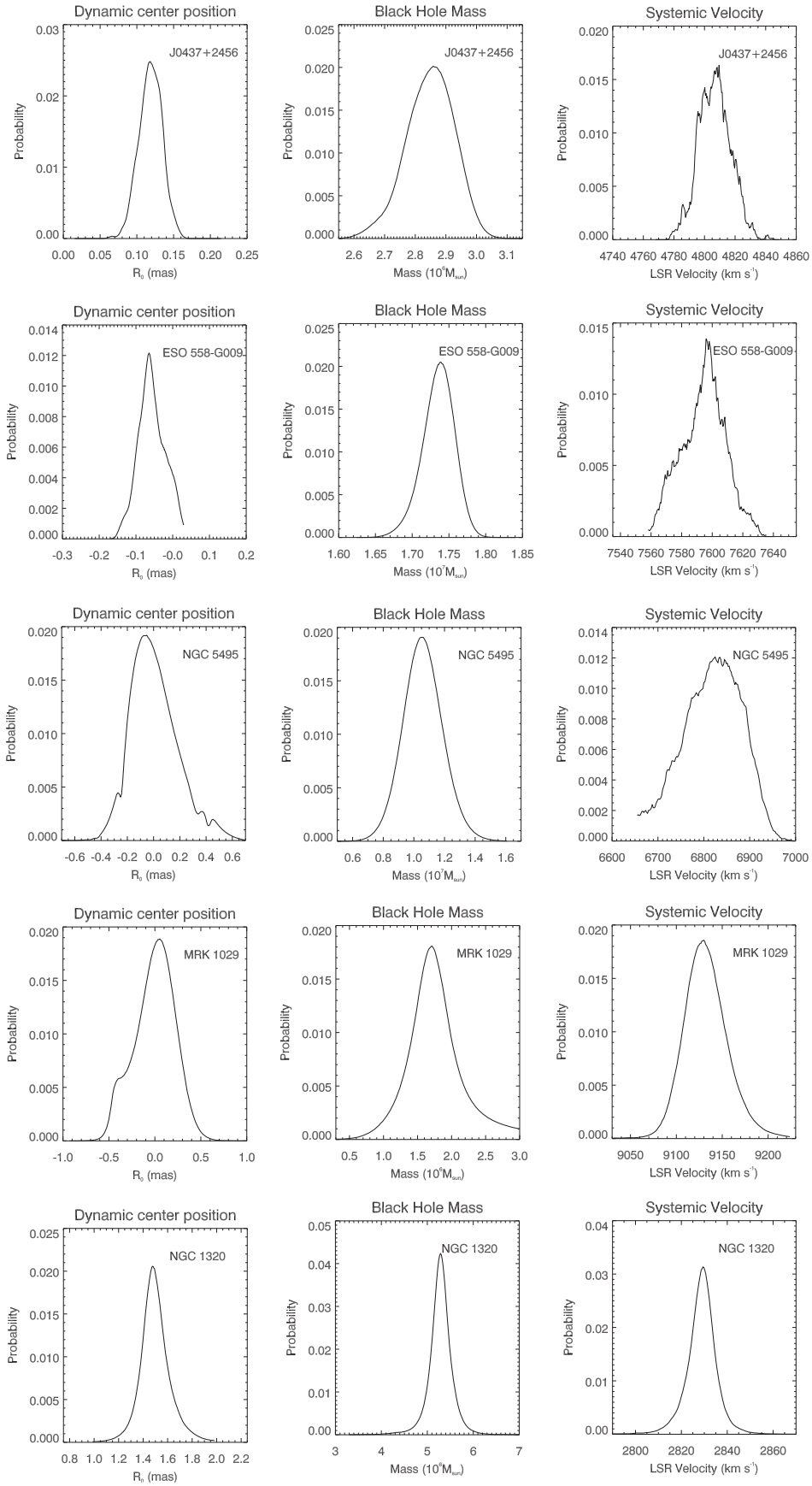

Figure 4. Probability density distribution for the fitted dynamical center position, black hole mass and recession velocity from the Bayesian fitting for the five galaxies in this study. The reduced χ^2 for the five galaxies are 1.07, 1.28, 0.22, 1.08 and 1.68, respectively. The small reduced χ^2 for NGC 5495 is likely due to small number of data points and an overestimation of the VLBI positional uncertainty. Please refer to the text for more details.

SMBH mass is ±5.8%. The dynamical center is located –0.051 mas from the original reference position (with velocity of 6789.03 km s^{-1}) on the major axis of the maser disk. Because we have a small number of data points, the reduced χ^2 is not a strong indicator of the goodness of fit, and in fact we get a value significantly less than unity. We suspect this is caused by the combination of both too few data points and overestimation of the VLBI positional uncertainties. As shown on the *P–V* diagram, the rotation curve is sparsely sampled by only a few data points. Overestimation of the positional uncertainties is indicated on the *P–V* diagram where the two rightmost redshifted features (close in velocity) are separated much less than their uncertainties in radius, horizontally. The VLBI positional uncertainties are estimated by the empirical relation of $0.5\Theta/(S/N)$, where Θ is the projected synthesized beam size and S/N is the signal-to-noise ratio. Due to the low declination of NGC 5495 and the north–south orientation of the maser disk, NGC 5495 has the largest projected synthesized beam among the five galaxies in this study. So the positional uncertainty calculated empirically might not correctly reflect the real uncertainty here. We show the PDF for the dynamical center position, the SMBH mass and the recession velocity in Figure 4.

3.2.4. MRK 1029

The GBT spectrum of Mrk 1029 (Figure 1) does not show the triple-peaked profile characteristic of disk systems such as J0437+2456, ESO 558–G009 and NGC 5495. Instead, there are only two prominent groups of spectral lines centered around 8980 and 9136 km s^{-1}. Two recession velocities are reported from NED for Mrk 1029 from optical measurements, 9076 ± 32 km s^{-1} (Huchra et al. 1999) and 9160 ± 61 km s^{-1} (de Vaucouleurs et al. 1991). The strongest maser line is at 9136.3 km s^{-1}. Our GBT spectrum also shows possible features located near 9550 and 10100 km s^{-1}, but our VLBI observation does not cover those velocities.

The colors in the VLBI map of Mrk 1029 in Figure 3 identify maser features between 9100 and 9220 km s^{-1} as the systemic masers and those between 9220 and 9300 km s^{-1} as the redshifted masers. Here we set a 5σ flux cutoff of 7 mJy beam^{-1} channel^{-1} with a channel width of 125 kHz. Masers are distributed linearly from the north–east to the south–west at a P.A. of 218° ± 10°, and the redshifted and blueshifted features are symmetric and roughly equidistant from the systemic features. We estimate the inclination angle of the disk to be 79° ± 2°.

To cope with the ambiguity in identifying the recession velocity, we averaged the two reported velocities above and use 9118 ± 50 km s^{-1} as a Gaussian prior in the Bayesian fitting. We also set a Gaussian prior of 0.0 ± 0.2 mas for the position of the dynamic center. Due to the ambiguity of maser origin in this galaxy, as some of them may not originate in the modeled disk, we used an "outlier-tolerant" method rather than Gaussian probabilities when calculating the probability of each model given the data (Reid et al. 2014). This would minimize the effects of deviated data in constraining the model, which is essential for us to reach a self-consistent result here.

We show the best-fit rotation curve and residuals in Figure 3, in which all the high-velocity features trace the Keplerian rotation well. The best-fit (with reduced χ^2 of 1.08) SMBH mass for MRK 1029 is $(1.7 \pm 0.45) \times 10^6 M_\odot$. The fitted recession velocity $V_0^{\rm LSR,opt}$ is 9129.9 ± 26.0 km s^{-1}. The uncertainty on the SMBH mass is ±27.5%. The dynamical center is located 0.05 mas from the original reference position (with velocity of 9136.86 km s^{-1}) on the major axis of the maser disk. We show the PDFs for the dynamical center position, the SMBH mass and the recession velocity in Figure 4.

Future H I observations of Mrk 1029 could better constrain the recession velocity and thereby aid in identifying the systemic masers. Also, the disk interpretation above could be verified if maser features redward of 9500 km s^{-1} could be mapped with future VLBI observations.

3.2.5. NGC 1320

As in Mrk 1029, the masers in NGC 1320 do not fall into the three distinct velocity groups that characterize a typical disk maser. In addition to imaging the maser distribution with the original channel spacing of 0.86 km s^{-1} (62.5 kHz), we also averaged the data over several velocity ranges to image faint, broad features. Figure 3 shows a map of features detected with S/N greater than 5. The maser distribution shows an east–west orientation, with a P.A. of 75° ± 10°. No systemic features (near the recession velocity of 2649 km s^{-1}) were detected in our VLBI observations, so we cannot estimate the inclination angle using the method described above. We note, though, that a strong maser feature appeared at the velocity of 2663.0 km s^{-1} in a later (2012 December 19) GBT spectrum. Several maser spots on both the blue and redshifted sides are offset from the major axis of the VLBI map, suggesting a strong warp or origin of masers different from disk. Nonetheless, the map is suggestive of a disk. The masers in NGC 1320 cover an angular size of ≈4 mas, equivalent to about 1.6 pc at a distance of 38 Mpc. This linear size is on the high end of the distribution of other maser disk sizes (as listed in Section 4.2).

Despite the departures from a characteristic maser disk, we fit the VLBI data of NGC 1320 with the same "error-tolerant" Bayesian fitting as we did for Mrk 1029. Figure 3 shows the best-fit rotation curve, in which most of the high-velocity features trace the Keplerian rotation well. The best-fit (with reduced χ^2 of 1.68) black hole mass is $(5.3 \pm 0.4) \times 10^6 M_\odot$ with recession velocity $V_0^{\rm LSR,opt}$ of 2829.2 ± 11.4 km s^{-1}. The dynamical center is located 1.5 mas from the original reference position (with velocity of 2545 km s^{-1}) on the major axis of the maser disk. We show the PDF for the dynamical center position, the SMBH mass and the recession velocity in Figure 4. As the maser profile is highly variable, future VLBI observations could potentially catch more systemic masers and high-velocity masers to enable a better characterization of the maser system in NGC 1320 (e.g., test for a warped disk).

3.3. Possible Sources of Systematic Error and Overall SMBH Masses

In addition to the formal fitting errors we estimated above, there are several other factors that contribute to the uncertainty in estimating the black hole mass. The SMBH mass depends directly on the galaxy distance, which we estimate from the Hubble law. So any departure from the pure Hubble flow will affect our distances and SMBH masses. A typical peculiar velocity of 300 km s^{-1} (e.g., Masters et al. 2006) would cause an uncertainty on the SMBH mass of 6.3% for J0437+2456,

3.9% for ESO 558–G009, and 4.4% for NGC 5495, to be added in quadrature.

In our fitting model, we assume that all high-velocity features lie on the mid-line of the disk. To account for departures from the mid-line, a velocity correction is needed when converting rotation velocity to the LOS velocity. Depending on the mass of the SMBH, the radius of the maser's orbit, and the angular departure from the mid-line, one may be able to detect LOS accelerations even for the high-velocity maser lines through spectral monitoring. For a high-velocity feature located away from the mid-line by an angle of ϕ, the LOS velocity would deviate from the Keplerian rotation velocity by about $1 - \cos(\phi)$. Since the deviation of maser features from the mid-line are more likely to be distributed between zero and the max angle $\phi_{\rm max}$, the mean deviation on the rotation velocity will be smaller than $1 - \cos(\phi_{\rm max})$. In the best measured disk maser galaxy NGC 4258, most of the high-velocity features lie within 5° from the mid-line, and the maximum deviation from the mid-line is 13° as shown by few maser features (Humphreys et al. 2008). If not corrected, a 13° deviation would introduce a 2.6% adjustment on the rotation velocity and a 5.2% under-estimation on the SMBH mass. (The uncertainty of the fitted black hole mass ΔM depends on the deviation of the velocity of the high-velocity features from the best-fit rotation curve ΔV as $\frac{\Delta M}{M} = \left(1 + \frac{\Delta V}{V}\right)^2 - 1$.)

In this paper we estimated the inclination angle i prior to the disk fitting, and then fixed it during the fitting to speed convergence. The effect of fitting the inclination angle is similar to the deviation of the high-velocity features from the mid-line, as a sin i factor is applied to the rotation velocity. The difference is that the inclination angle is a systematic effect on all rotation velocities and it causes an underestimate of the SMBH mass. The inclination angle of the maser disks currently known are all close to perfectly edge-on ($i = 90°$) with a typical deviation of 10° (in the best measured case of NGC 4258, the inclination angle at the radius of the systemic masers is about 81.°7 (Humphreys et al. 2013)). In our study, the typical deviation from edge-on is 10°, which corresponds to a change of rotation velocities by 1.5% and the fitted black hole mass by 3% from a perfectly edge-on system.

As mentioned in Section 2.2, the absolute positional uncertainty of the reference feature in "self-calibration" observations may induce a systematic positional uncertainty for each maser spot. This positional uncertainty is given by $(\Delta\nu/\nu_i)\theta_{\rm ref}$ (Thompson et al. 2001). Here the frequency for maser feature i is ν_i, where $\Delta\nu$ is the frequency difference between the reference feature and feature i, and $\theta_{\rm ref}$ is the positional uncertainty of the reference feature. The resulting positional uncertainties should be added in quadrature to the formal fitting uncertainty for each maser spot. For ESO 558–G009, the positional uncertainty of the reference feature is 72 mas. Considering the typical frequency difference of 40 MHz, this gives a positional uncertainty of 0.13 mas. We have added this uncertainty in quadrature to the formal fitting uncertainty for each maser spot, and the fitted SMBH mass remains $1.70 \times 10^7\,M_\odot$, with the uncertainty increased to 2.3%. For NGC 5495, the positional uncertainty of the reference feature is about 300 mas, with a typical frequency difference of 30 MHz, the additional positional uncertainty is about 0.4 mas. These yield a SMBH mass of $1.04 \times 10^7\,M_\odot$, with the uncertainty increased to 17%. Because of the uncertain nature of the maser structures in NGC 1320 and Mrk 1029, we did not include the position uncertainty in the estimates of their SMBH masses.

Finally, adding all the systematic uncertainties mentioned above, the SMBH mass results are $(2.9 \pm 0.3) \times 10^6\,M_\odot$ (9.2%) for J0437+2456, $(1.7 \pm 0.1) \times 10^7\,M_\odot$ (7.5%) for ESO 558–G009, and $(1.1 \pm 0.2) \times 10^7\,M_\odot$ (18.6%) for NGC 5495. We list the final fitting results for the 5 galaxies in Table 4.

4. DISCUSSION

4.1. The "Clean" Disk Data set

Here we compile a sub-sample of VLBI-confirmed, "clean" disk maser galaxies from the disk maser sample listed in Pesce et al. (2015), and we provide the SMBH mass and the inner and outer radius of the maser disk for each galaxy, as listed in Table 5. We define a clean disk as requiring that (1) the P–V diagram derived from VLBI observations is consistent with Keplerian rotation and (2) all the maser components come from the disk, with no jet or outflow contamination. Based on these criteria, NGC 1068, Circinus, NGC 4945, NGC 1386 and NGC 3079 are not included in our list. The purpose of the list is not to be as complete as possible, but to identify a physically homogeneous sample. Our final list contains 15 sources, including the 7 from Kuo et al. (2011), 3 from this work (J0437+2456, ESO 558–G009, and NGC 5495), NGC 4258 (Humphreys et al. 2013), NGC 3393 (Kondratko et al. 2008), NGC 5765b (Gao et al. 2016), IC 2560 (J. Wagner et al. 2016, in preparation) and UGC 6093 (W. Zhao et al. 2016, in preparation).

We note that uncertainties on the SMBH mass are not calculated in the same way for the whole "clean" disk sample, in which sources from Kuo et al. (2011) are calculated as this work, NGC 4258 and NGC 5765b are analyzed using the 3-D modeling of the disk, while the uncertainties reported for NGC 3393, IC 2560 and UGC 6093 are just formal fitting errors. So we calculated the systematics mentioned in Section 3.3 for NGC 3393, IC 2560 and UGC 6093 and add them in quadrature to their formal fitting error, except for the uncertainty caused by absolute position uncertainty of the reference maser feature. The SMBH mass uncertainties listed in Table 5 contain these systematics.

4.2. Estimation of the Maser Disk Radii from both Single-dish Spectra and VLBI Maps

Our use of the single-dish spectra is complementary to the VLBI data, in the sense that even though single-dish spectra do not provide spatially resolved constraints of the position of maser spots, the sensitivity level reached in stacked single-dish observations is usually higher than VLBI due to more available observations. For our study, all 15 sources listed in the "clean" disk sample have multiple single-dish observations with the GBT (with a typical 1σ noise level of less than 1 mJy per 24.4 kHz after combining all the data), while usually the imaging sensitivity reached in VLBI observations is between 5 and 10 mJy per beam per 125 kHz. So there might be more extended emission revealed in the single-dish spectra, that is not picked up by our VLBI observations.

We used single-dish spectra from Pesce et al. (2015), which has combined all available GBT spectra for each of the 15 sources, thus providing unprecedented sensitivity. We estimate the maser disk radii with $r_{\rm edge} = \frac{GM}{(V_{\rm edge} - V_0)^2}$, where M is the

Table 5
The Maser Disk Size, SMBH Mass, and Luminosity from the "Clean" Disk Sample

Name	SMBH Mass ($10^7 M_\odot$)	Dist. (Mpc)	R_{in} (pc)	R_{out} (pc)	Log L_{WISE^*} (erg s^{-1})	Log $L_{WISE5''.5}$ (erg s^{-1})	Log $L_{[O\ III]}$ (erg s^{-1})	References (for Columns 2, 8)
(1)	(2)	(3)	(4)	(5)	(6)	(7)	(8)	(9)
NGC 4258	4.00 ± 0.09	7.60	0.11 ± 0.004	0.29 ± 0.01	40.87	40.94	38.77	3, 10
NGC 4388	0.84 ± 0.09	19.0	0.24 ± 0.03	$^*0.29^{+0.27}_{-0.03}$	42.00	42.08	40.40	1, 9
NGC 2273	0.75 ± 0.05	25.7	0.03 ± 0.01	$^*0.084^{+0.282}_{-0.013}$	42.19	42.26	40.50	1, 9
IC 2560	0.44 ± 0.09	44.5	0.11 ± 0.02	0.47 ± 0.03	42.44	42.50	41.00	8, 9
UGC 3789	1.04 ± 0.06	45.4	0.08 ± 0.02	$^*0.30^{+0.19}_{-0.03}$	42.07	42.16	41.30	2, 9
NGC 1194	6.5 ± 0.4	53.2	$^*0.54^{+0.03}_{-0.25}$	$^*1.33^{+0.97}_{-0.06}$	42.61	42.68	39.90	1, 9
NGC 3393	3.10 ± 0.37	56.2	0.17 ± 0.02	$^*0.60^{+0.80}_{-0.04}$	42.37	42.44	41.30	7, 9
J0437+2456	0.29 ± 0.03	65.3	0.06 ± 0.03	0.13 ± 0.03	41.56	41.65	39.00	5, 11
NGC 2960	1.16 ± 0.07	72.2	0.13 ± 0.04	$^*0.37^{+0.71}_{-0.04}$	42.29	42.38	40.50	1, 9
NGC 5495	1.05 ± 0.20	95.7	0.10 ± 0.05	0.30 ± 0.05	42.23	42.36	39.80	5, 12
NGC 6323	0.94 ± 0.04	106.0	0.13 ± 0.05	0.30 ± 0.05	42.11	42.22	40.40	1, 9
ESO 558–G009	1.70 ± 0.14	107.6	0.20 ± 0.05	0.47 ± 0.06	42.38	42.46	⋯	5, ⋯
NGC 5765b	4.55 ± 0.31	117.0	0.30 ± 0.06	1.15 ± 0.07	43.16	43.24	41.10	4, 11
NGC 6264	2.91 ± 0.11	139.4	0.24 ± 0.07	0.80 ± 0.07	42.23	42.29	41.30	1, 9
UGC 6093	2.65 ± 0.23	153.2	0.12 ± 0.07	$^*0.24^{+0.29}_{-0.08}$	41.88	42.01	40.20	6, 11

Note. Column (1): Galaxy name. Column (2): SMBH masses. We have added systematic errors to the uncertainties of NGC 3393, IC 2560 and UGC 6093. See the text for more details. Column (3): Distances, taken from NED using the Hubble flow, except for NGC 4258 and NGC 4388. The distance for NGC 4258 is adopted from Humphreys et al. (2013). We adopted the distance for NGC 4388 from Kuo et al. (2011). Column (4): Maser disk inner radius. Column (5): Maser disk outer radius. The maser disk size comes from Table 6. Radius starts with an asterisk indicates the radius estimated from VLBI are not consistent with results from single-dish spectrum, within 3σ, so we use the VLBI radius as the final value, with 1σ uncertainty covering the difference between VLBI and single-dish measured results. Column (6): 12 μm luminosity measured from the central pixel on the *WISE* Band 3 image. Column (7): 12 μm luminosity measured from $5''.5$ aperture photometry reported from *WISE* online catalog. Column (8): Optical O [III] luminosity from literature.

References. (1) Kuo et al. (2011), (2) Reid et al. (2013), (3) Humphreys et al. (2013), (4) Gao et al. (2016), (5) this work, (6) W. Zhao et al. (2016, in preparation); (7) Kondratko et al. (2008) (8) J. Wagner et al. (2016, in preparation), (9) Greene et al. (2010) (10) Ho et al. (1997) (11) SDSS online catalog; (12) J. E. Greene (2016, private communication).

measured SMBH mass, V_0 is the best-fit recession velocity of the SMBH from VLBI data, V_{edge} are the velocity boundaries (identified with S/N of maser feature's intensity greater than 5), corresponding to the minimum and maximum Keplerian rotation velocity on both the redshifted and blueshifted side. From this we get the inner and outer radii of both the redshifted and blueshifted masers, and we select the minimum and maximum radii for the high-velocity masers. We estimate uncertainties in maser disk radii from both the SMBH mass measurement and the fitted recession velocity. Here we added a 5.5% uncertainty on the SMBH mass in quadrature to the formal fitting error to account for the uncertainty on the galaxy distance.[15] We note that this radius estimation is based on the assumptions that all masers we included trace the Keplerian rotating disk and they are also located on the mid-line of the edge-on disk. These assumptions could be violated by maser flares or masers generated from outflows.

From our VLBI maps, we estimate the range of radii for the systemic masers and high-velocity masers separately. For the high-velocity masers, we measure the projected separation between the maser positions and the fitted dynamical center, directly. Uncertainties on the maser radii come from position uncertainties on the maser spots themselves and the uncertainties on the distances to the galaxies. For the distance calculation, we also apply a 5.5% uncertainty on H_0, as mentioned above. For the systemic masers, there are two ways to estimate the radius. First, if the accelerations (velocity drift with time) of the systemic features have been measured from spectral monitoring, we apply that together with the measured SMBH mass to constrain the radius as $r = \sqrt{\frac{GM}{a}}$. Second, the radius can be estimated from the slope of the systemic features on the P–V diagram, $\Omega = \sqrt{\frac{GM}{r^3}}$. The second method does not work well if the systemic features are distributed over a large range of radii, as different slopes on the P–V diagram will blend together. So here we use the first method when applicable.

Finally, we compare the maser disk radii estimated from both single-disk spectrum and the VLBI maps. If the two results are consistent within 3σ, we use the radius derived from VLBI as the final value. Otherwise we still apply the VLBI result as the final value, but we add the difference between the two methods in the uncertainties. We note that the inner radii estimated from the two methods are consistent in all other galaxies except NGC 1194. And NGC 3393 remains the only case where the inner radius estimated from the systemic masers is significantly smaller than that estimated from high-velocity VLBI map, as originally reported in Kondratko et al. (2008). For the outer radius, inconsistency is seen in NGC 4388, NGC 2273, NGC 1194, NGC 3393, UGC 3789, NGC 2960 and UGC 6093. In the first four of these galaxies, the single-dish spectrum shows a continuous maser distribution between the high-velocity features and systemic features (see Figure 1 in Pesce et al. 2015), making it difficult to assign the velocity range associated with the maser disk. We list the inner and outer radii for each maser disk in Table 5. Radii that show inconsistency between the single-dish spectrum estimation and

[15] We consider two recent results on H_0, which are 73.24 ± 1.74 km s^{-1} Mpc^{-1} (Riess et al. 2016) and 67.8 ± 0.9 km s^{-1} Mpc^{-1} (Planck Collaboration et al. 2016) to arrive at the conservative estimate of 5.5% uncertainty on H_0.

Table 6
The Maser Disk Size Measured with Different Methods from the "Clean" Disk Sample

Name	V_{sys} (km s^{-1})	R_{in}^{V-sys} (pc)	R_{in}^{V-hi} (pc)	R_{in}^{S} (pc)	R_{out}^{V-sys} (pc)	R_{out}^{V-hi} (pc)	R_{out}^{S} (pc)	References (for VLBI Results)
(1)	(2)	(3)	(4)	(5)	(6)	(7)	(8)	(9)
NGC 4258	474	0.14 ± 0.002	0.11 ± 0.004	0.12 ± 0.003	0.15 ± 0.002	0.29 ± 0.01	0.31 ± 0.01	3
NGC 4388	2527	⋯	0.24 ± 0.03	0.21 ± 0.02	⋯	0.29 ± 0.03	0.56 ± 0.06	1
NGC 2273	1832	⋯	0.03 ± 0.01	0.03 ± 0.002	⋯	0.08 ± 0.01	0.37 ± 0.04	1
IC 2560	2906	0.08 ± 0.006	0.11 ± 0.02	0.09 ± 0.01	0.087 ± 0.01	0.47 ± 0.03	0.54 ± 0.08	8
UGC 3789	3262	0.08 ± 0.002	0.08 ± 0.02	0.06 ± 0.004	0.22 ± 0.01	0.30 ± 0.03	0.49 ± 0.06	2
NGC 1194	4051	0.44 ± 0.01	0.54 ± 0.03	0.29 ± 0.02	1.38 ± 0.04	1.33 ± 0.06	2.30 ± 0.02	1
NGC 3393	3750	0.16 ± 0.01	0.36 ± 0.02	0.30 ± 0.02	0.176 ± 0.01	0.64 ± 0.04	1.40 ± 0.11	7
J0437+2456	4807	0.07 ± 0.003	0.04 ± 0.03	0.06 ± 0.01	0.126 ± 0.01	0.13 ± 0.03	0.15 ± 0.02	5
NGC 2960	4945	⋯	0.13 ± 0.04	0.11 ± 0.01	⋯	0.37 ± 0.04	1.08 ± 0.16	1
NGC 5495	6839	⋯	0.10 ± 0.05	0.08 ± 0.02	⋯	0.30 ± 0.05	0.48 ± 0.23	5
NGC 6323	7848	0.16 ± 0.003	0.13 ± 0.05	0.12 ± 0.01	0.40 ± 0.01	0.30 ± 0.05	0.35 ± 0.03	1
ESO 558–G009	7597	0.20 ± 0.01	0.20 ± 0.05	0.21 ± 0.02	0.341 ± 0.01	0.47 ± 0.06	0.49 ± 0.05	5
NGC 5765b	8335	0.39 ± 0.01	0.30 ± 0.06	0.29 ± 0.02	0.88 ± 0.03	1.15 ± 0.07	1.29 ± 0.09	4
NGC 6264	10213	0.18 ± 0.003	0.24 ± 0.07	0.20 ± 0.01	0.425 ± 0.01	0.80 ± 0.07	0.99 ± 0.09	1
UGC 6093	10828	⋯	0.12 ± 0.07	0.11 ± 0.01	⋯	0.24 ± 0.08	0.53 ± 0.04	6

Note. Estimation of the maser disk radii from both single-dish spectrum and VLBI map. When possible, we also estimate the range of radii that systemic masers span by either using the acceleration data or slope on the position–velocity diagram. Refer to Section 4.2 for details. Column (1): galaxy name. Column (2): recession velocity derived from VLBI. Column (3): the inner radius calculated from systemic masers from VLBI. Column (4): the inner radius calculated from high-velocity masers in VLBI. Column (5): the inner radius calculated from single-dish spectrum. Column (6): the outer radius calculated from systemic masers from VLBI. Column (7): the outer radius calculated from high-velocity masers in VLBI. Column (8): the outer radius calculated from single-dish spectrum.
References. (1) Kuo et al. (2011), (2) Reid et al. (2013), (3) Humphreys et al. (2013), (4) Gao et al. (2016), (5) this work, (6) W. Zhao et al. (2016, in preparation), (7) Kondratko et al. (2008), (8) J. Wagner et al. (2016, in preparation).

VLBI results are marked by an asterisk. The original measured radii for each galaxy from both methods are listed in Table 6.

4.3. SMBH Mass versus Maser Disk Size

Disk masers provide the best measured extragalactic SMBH masses (e.g., Kormendy & Ho 2013; Miyoshi et al. 1995; Kuo et al. 2011; this work). However, the low detection rate even in type 2 AGN (<1%, J. A. Braatz et al. 2016, in preparation) prevents accumulating a large sample. To improve the efficiency of future surveys, several studies have tried to correlate the incidence of maser emission with host galaxy properties, either in the optical (Zhu et al. 2011; Constantin 2012; van den Bosch et al. 2016), radio (Zhang et al. 2012) or X-ray (Zhang et al. 2006, 2010), but no clear conclusion has been made. A better understanding of the mechanism that generates disk masers will also provide important guidance for future disk maser surveys. Below we concentrate on the mechanisms that determine the inner and outer radius of the maser disk.

Theoretical models have been put forth to explain the generation of maser emission around a SMBH. Neufeld et al. (1994) proposed that X-ray emission from the central AGN provides the heating that generates a suitable environment for population inversion and maser emission. In their model, X-rays irradiate the slightly tilted and warped molecular disk, which is formed on the outer part of the accretion disk. As the molecular layer is heated, the abundance of H_2O molecules increases. With the molecular hydrogen density between 10^7 and 10^{11} cm^{-3}, gas temperature between 400 and 1000 K and water abundance $x(H_2O) = n(H_2O)/n(H_2) \gtrsim 10^{-4}$, luminous maser emission can be generated. Based on standard accretion disk theory (Shakura & Sunyaev 1973), Neufeld & Maloney (1995, hereafter NM95) suggested that the outer radius for masing is determined by a phase transition from molecular to atomic gas, while the inner radius is caused by the flattening of the disk, making it no longer exposed to the central X-ray source. So the gas there would be too cold to pump masers. Collison & Watson (1995) include dust grains in their calculation of maser emissivity and show that cold dust (with respect to warm molecular gas) is essential for maintaining maser emission. Based on these studies, the AGN's luminosity, the inclination and warp of the disk, and the gas and dust content of the molecular disk together determine the radii at which maser emission forms.

Wardle & Yusef-Zadeh (2012, hereafter WY12) reported an upper envelope to the disk maser outer radii, which scales with SMBH mass as $R_{out} \approx 0.3M_7$ pc (with $M = M_7 \times 10^7 M_\odot$), based mainly on the results of Kuo et al. (2011). To better explore the relation between SMBH mass and maser disk size, here we fit the inner and outer radius of the maser disk with the SMBH mass in the the form of $\mathrm{Log}(R) = \alpha \mathrm{Log}(M) + \beta \pm \epsilon$. We note that the uncertainties on the measured inner and outer radius of NGC 4258 are about an order of magnitude smaller than in other sources, making NGC 4258 dominate any linear fitting result and possibly suppressing any general trend between maser disk size and SMBH mass. Nevertheless, we calculate the Spearman's rank correlation coefficient ρ_S for the inner and outer radius case, giving 0.71 and 0.62, respectively. Their two-tail probability are 0.01 in both cases. Since these coefficients do suggest the existence of some correlation, here as a preliminary check, we fit the data with equal uncertainties (uniform weighting) on the maser disk radius between different sources and get:

$$\mathrm{Log}(R_{in}/\mathrm{pc}) = (0.60 \pm 0.17) \times \mathrm{Log}(M_{SMBH}/M_\odot) - (5.21 \pm 1.17) \pm 0.22$$

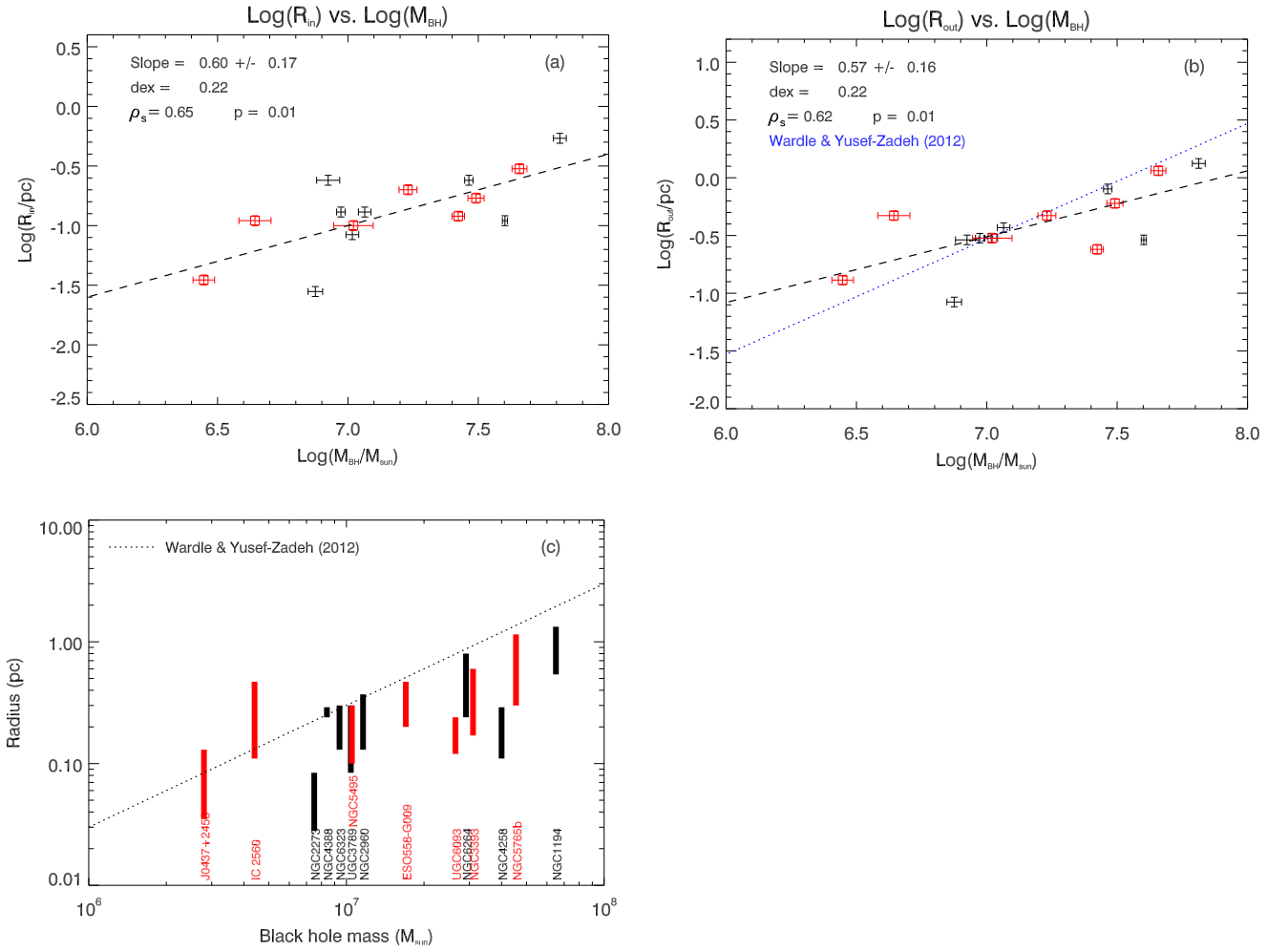

Figure 5. Relation between the maser disk radius and the central SMBH mass. Maser disks reported in Kuo et al. (2011) are shown in black, while new results are shown in red. We show the inner and outer radius of maser disks vs. SMBH mass in plots (a) and (b), with the best-fit result with uniform weighting shown as the black dashed line, while the blue dotted line in plot (b) shows the scaling relation reported in Wardle & Yusef-Zadeh (2012). We also show the maser disk extension (from the inner to the outer radii, as shown by the vertical bars) vs. SMBH mass, following the plot style in Wardle & Yusef-Zadeh (2012), in plot (c). The dotted line also shows the scaling relation of the outer radius of maser disks vs. SMBH mass as reported in Wardle & Yusef-Zadeh (2012).

$$\mathrm{Log}(R_{\rm out}/\mathrm{pc}) = (0.57 \pm 0.16) \times \mathrm{Log}(M_{\rm SMBH}/M_{\odot}) - (4.50 \pm 1.17) \pm 0.22.$$

We show the fitting results in Figures 5(a) and (b) respectively, in which the black dashed line shows the best-fit result in both cases, while the blue dotted line in Figure 5(b) shows the relation from WY12. For direct comparison to WY12, we show the extent of the maser disks by the vertical bars in Figure 5(c). Targets from Kuo et al. (2011) are shown in black, while others are shown in red. The black dotted line marks the relation from WY12. We do not include Sgr A*, which is used in WY12 but does not have disk masers.

In general, new results from this work and others strengthen the empirical upper envelope reported in WY12 (as shown in Figure 5(c)), although the slope we get for the outer radii under uniform weighting is not consistent with the slope of 1.0, which was used in WY12. And we note that although NM95 derived $R_{\rm out} \propto L_{41}^{-0.426} M_8^{0.617}$ (Equation (4) in NM95), which is consistent with our fitting results, their model was based on the assumption of steady accretion from the pc-scale maser disk to the central SMBH, which may not be valid in disk maser galaxies (e.g., Gammie et al. 1999).

The SMBH mass sets an additional constraint on the inner radius of the maser disk. Maser amplification requires not only spatial alignment of molecular clouds along the gain path, but also velocity coherence along the LOS. The typical velocity coherence for the 22 GHz H_2O disk maser is about 1 km s^{-1} (the typical linewidth seen in disk masers). Velocity coherence path lengths shorten at smaller disk radii, as the rotation velocity increases. Gao et al. (2016) show $R_{\rm in} \propto M_{\rm SMBH}$ under such velocity coherence requirement. However, this differs from the fit determined above. So we conclude that the inner radius of the maser disk may not be determined solely by velocity coherence.

4.4. An Empirical Relation between WISE Luminosity and Maser Disk Outer Radii

As mentioned above, an AGN luminosity may determine the range of radii over which water masers amplify. Below we examine the relation between maser disk size and AGN luminosity. [O III] and X-ray 2–10 keV luminosity are often used as indicators for the isotropic AGN luminosity (e.g., Zakamska et al. 2003; Heckman et al. 2004; Liu et al. 2009). For the 15 galaxies in our "clean" disk maser sample, only 9

have 2–10 keV X-ray measurements (Masini et al. 2016; Castangia et al. 2013 and references therein), and 14 have [O III] measurements (Table 5). Most of our disk maser galaxies are Compton thick and 3 of the 9 X-ray measurements have only a lower limit on the intrinsic column density, which affects the estimation of the intrinsic X-ray luminosity. The [O III] data may suffer from intrinsic reddening (Greene et al. 2010). So besides using [O III] and X-ray data, here we explore the use of the *Wide-Field Infrared Survey Explorer* (*WISE*) Band 3 ($\lambda = 12\,\mu$m) luminosity (Wright et al. 2010) as an approximation for the AGN luminosity.

We choose the Band 3 data over other bands (3.4, 4.6 and 22 μm) for two reasons. First, there is a significant contribution from stellar photospheric emission at wavelengths shorter than 10 μm (e.g., Fu et al. 2010). Second, we can estimate the AGN bolometric luminosity L as $L = \int L_\nu d\nu = \int L_\lambda d\lambda \approx \lambda L_\lambda$ near $\lambda = 10\,\mu$m when $U \geqslant 10^7$ (Draine & Li 2007), where U is the radiation parameter. See the Appendix below for the derivation of U in disk maser galaxies.

The spatial resolution of *WISE* at Band 3 is about 7.4. To eliminate contamination from star formation regions in the host galaxy, we use the 5.″5 aperture photometry archive data, which has the smallest aperture among the *WISE* data sets and best match the Band 3 resolution. We also measure the background subtracted flux from the central pixel from the *WISE* Band 3 online image. Each pixel covers 1.″375 on the image. Galaxies in our sample have distances between 7.6 and 153.2 Mpc, so the pixel size ranges from 50 pc to 1 kpc. To test whether the observed IR emission originates from the AGN, we examine the *WISE* color–color plot (W1–W2 versus W2–W3) for our disk maser sample (Figure 6). For guidance, we plot the color–color "wedge" that luminous AGN may fall in (Mateos et al. 2012) and the empirical mid-infrared criterion for AGN identification, which is W1–W2 of 0.8 (Stern et al. 2012), in dotted line. Clearly most of our disk maser galaxies do not fall in the wedge nor do they lie above the W1–W2 of 0.8 line. This is not surprising as the completeness of the color–color wedge selection is a strong function of X-ray luminosity, as stated in Mateos et al. (2012). Below 10^{43} erg s^{-1}, where all nine disk maser galaxies with published X-ray measurements are located (Masini et al. 2016, Castangia et al. 2013), the *WISE* color–color wedge only selects less than 20% of type 2 AGN (Mateos et al. 2012). The majority of disk maser galaxies in our sample have W2–W3 between 2 and 3, and W1–W2 near zero. Comparing with the color–color diagram for different types of sources as shown in Yan et al. (2013), we see our *WISE* luminosities may have contamination from star formation and we cannot distinguish that from AGN emission.

Nevertheless, our logic here is that if we can see any correlations between the "star formation contaminated" *WISE* luminosity and maser disk properties (e.g., inner and outer radius), then such correlation should be strengthened when the intrinsic luminosity from the AGN has been used instead, as star formation activities should not affect the generation of maser emission. So we plot the inner and outer maser disk radii against the *WISE* Band 3 luminosity measured from both the peak pixel and 5.″5 aperture in the middle and bottom panel in Figure 6, respectively.

These plots suggest a correlation between the outer disk radius and the *WISE* luminosity, both in the peak pixel data and the 5.″5 aperture data. Here we calculate the Spearman's rank correlation coefficient ρ_S as a non-parametric test, giving 0.83 with the two-tail probability of 0.0001 for both cases. Such a high coefficient suggests a positive correlation. In contrast, no clear correlation is found between the inner disk radius and the *WISE* luminosity. The calculated Spearman's rank correlation coefficient is 0.53 with the p-value of 0.04, which disfavor a correlation.

To better characterize the correlation between the outer radius and the *WISE* luminosity, here we fit the data in the the form of $\mathrm{Log}(R) = \alpha \mathrm{Log}(L) + \beta \pm \epsilon$. Similar to the previous section, here we assign a 10% uncertainty for the disk radius in each galaxy, which gives equal weighting for all galaxies in the fitting. This would avoid NGC 4258 dominant the fitting and yields results with unreasonably high confidence levels. The best-fit results using the peak pixel data is:

$$\mathrm{Log}(R_{\rm out}/\mathrm{pc}) = (0.37 \pm 0.14) \times \mathrm{Log}(L_{\rm WISEW3}/(\mathrm{erg\ s^{-1}})) - (16.19 \pm 6.00) \pm 0.25.$$

The fit from the *WISE* 5.″5 aperture data is consistent with that from the peak pixel data. However, both fits are strongly influenced by a small number of data points at the low and high ends of the luminosity distribution. We show the results on the middle and bottom panel of Figure 6.

We also calculate ρ_S between the maser disk size and both the absorption-corrected 2–10 keV luminosity and [O III] luminosity, though they are all less than 0.5, suggesting no evident correlation. We show these results in Figure 7. To investigate further, here we compare the 2–10 keV luminosity and [O III] luminosity against *WISE* luminosity in Figure 8. In general, there is a good consistency between the X-ray data and *WISE* data, though the small number of available X-ray measurements prevents a more systematic comparison. As for the [O III] data, the overall offset and scatter may reflect the uncorrected reddening, as only Galactic absorption has been corrected in the [O III] data here.

Masini et al. (2016) also compared the inner and outer radii of maser disks in a sample of 14 maser galaxies to the X-ray 2–10 keV luminosity measured from the *Nuclear Spectroscopic Telescope Array* (*NuSTAR*), and they did not find a correlation. Though we note that several "non-clean" disk masers have been included in their study (e.g., NGC 1068, NGC 1386, NGC 3079, NGC 4945 and Circinus). Besides, the X-ray luminosities we used here are measured by either XMM or *Chandra* at the wavelength roughly between 0.1 and 10 keV, whereas *NuSTAR* covers the higher energy band between 3 to 79 keV, which is less sensitive to absorption and thus not good coping with absorption corrections. Nevertheless, our current result and results from Masini et al. (2016) do not suggest the existence of correlation between maser disk size and X-ray luminosity. Considering the good consistency between the X-ray data and *WISE* data we mentioned above, a larger sample of disk masers with X-ray measurements would be better to verify the correlation between maser disk size and AGN luminosity here.

One way to interpret the $R_{\rm out}$–L_{WISE} correlation is that since we see a tentative correlation between maser disk size and SMBH mass (as in previous section), and it is well known that SMBH mass correlates with galaxy bulge mass (e.g., Kormendy & Ho 2013), which can convert to bulge luminosity. So we might expect a correlation between maser disk size and mid-infrared luminosity, if it contains luminosity from both the AGN and the galaxy bulge. However, this interpretation might not hold true, since we also see a correlation between $R_{\rm in}$ and

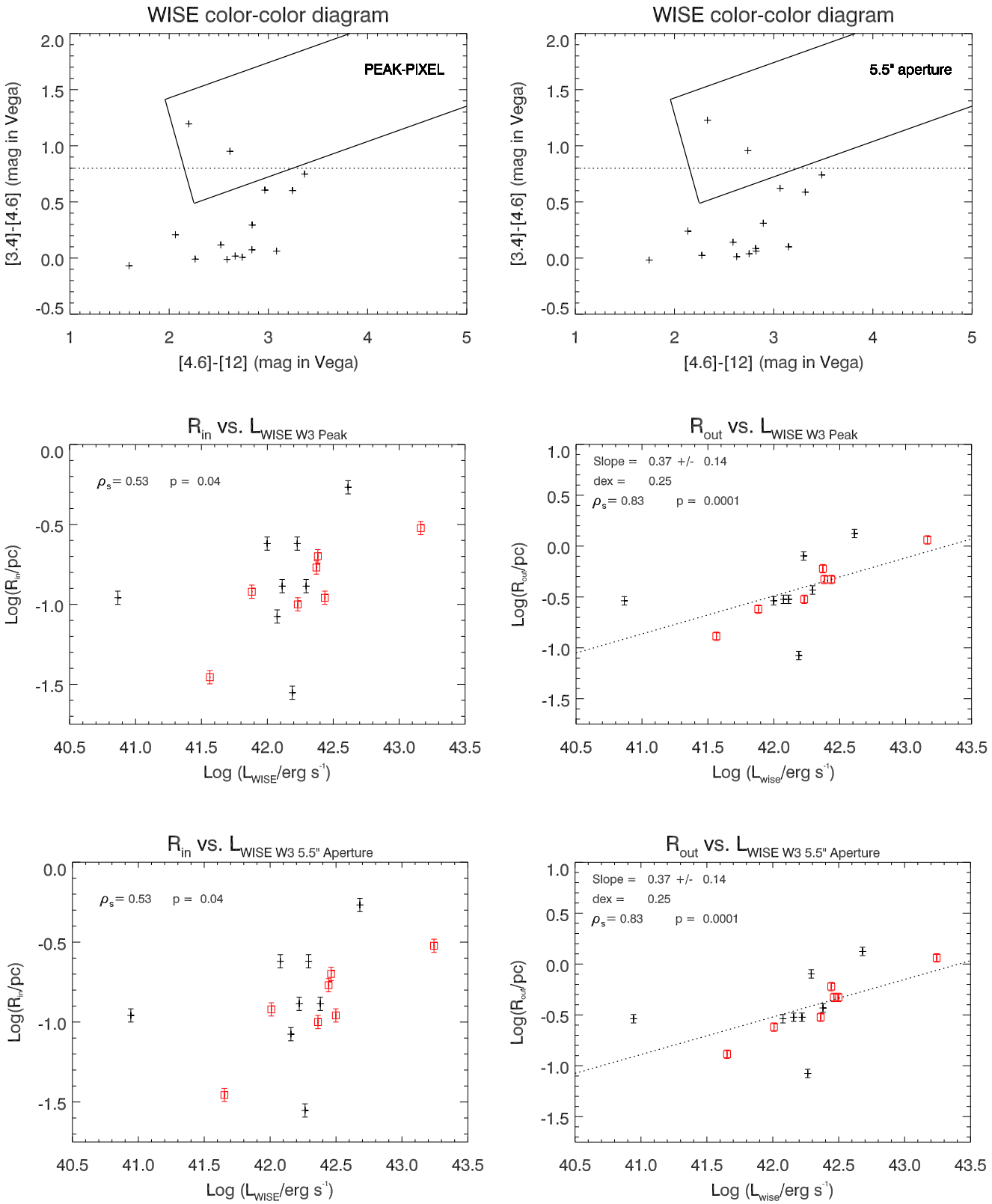

Figure 6. In the upper panel we show the *WISE* color–color plot (W1–W2 vs. W2–W3) for our disk maser sample for both the central pixel photometry case and the 5.″5 aperture photometry case to help identify their MIR-radiation origin. For guidance, we plot the color–color wedge that luminous AGN may fall in from Mateos et al. (2012) in solid lines and the W1–W2 of 0.8 in dotted line (Stern et al. 2012). Only NGC 1194 and NGC 4388 in our sample fall within the color–color wedge. Plots on the middle and bottom panel show the relation between inner and outer radii of maser disks with AGN luminosity measured from *WISE* W3 (12 μm) peak pixel and 5.″5 aperture photometry. Maser disks reported in Kuo et al. (2011) are shown in black cross, while new results are shown in red open square. The dotted line in the right panels indicate the best-fit results, under uniform weighting. In the upper left corner in each subplot, we give the Spearman's rank correlation coefficient ρ_S together with the two-side possibility p-value. The best-fit slope and scatter are also shown when possible.

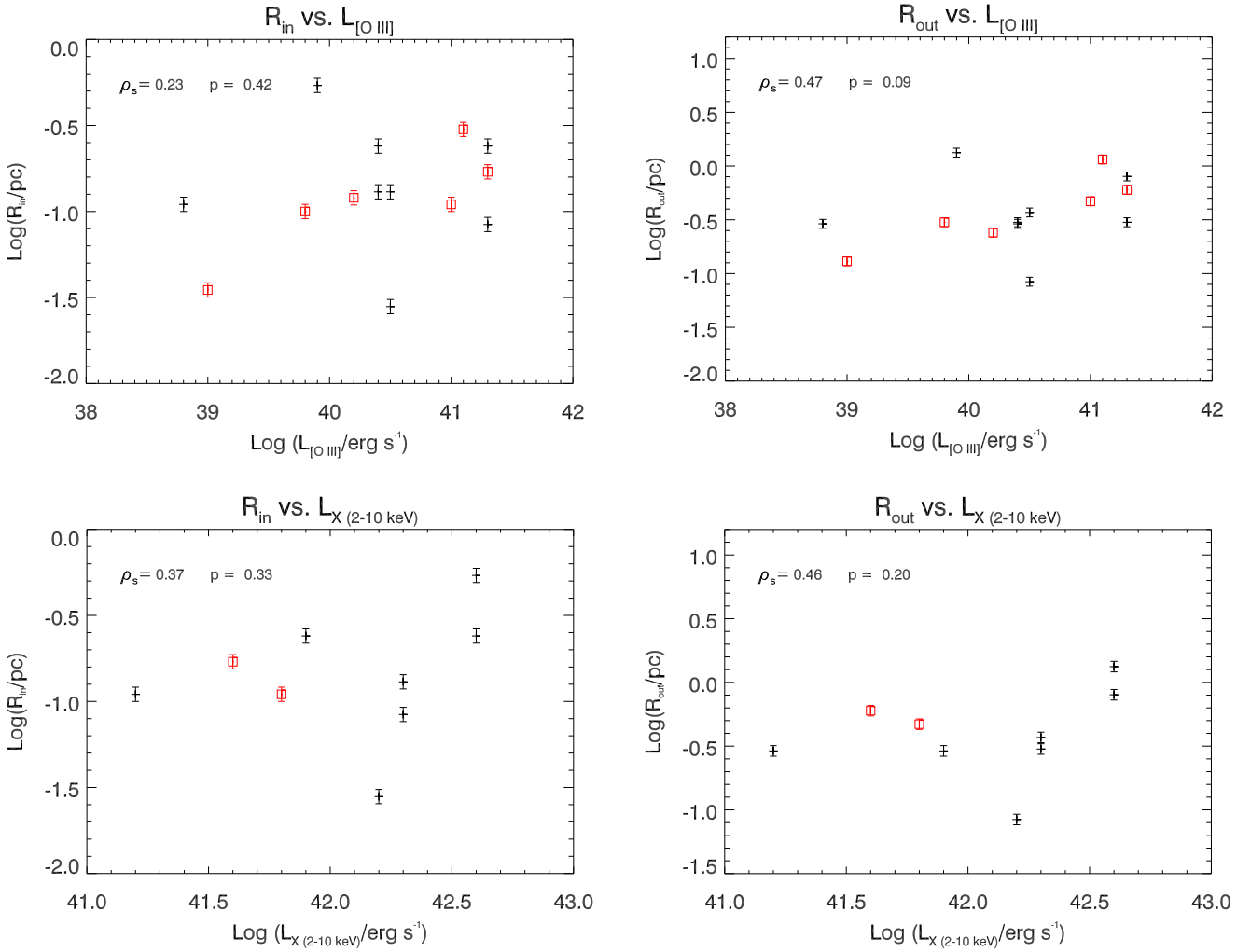

Figure 7. Correlation between inner and outer radii of maser disks with AGN luminosity measured from [O III] and X-ray 2–10 keV data. Maser disks reported in Kuo et al. (2011) are shown in black cross, while new results are shown in red open square, when their [O III] or X-ray measurements are available. we give the Spearman's rank correlation coefficient ρ_S together with the two-side possibility p-value.

SMBH mass but we do not see a strong correlation between $R_{\rm in}$ and L_{WISE} here.

As we have derived in the Appendix, if the outer radius of the maser disk is constrained by the molecular gas kinematic temperature as it approaches $T_{\rm min} \approx 400$ K, the slope derived between $R_{\rm out}$ and mid-infrared luminosity should be 0.5, with an intercept of 22.18. Our current best-fit result is consistent with such a slope and intercept, but a larger sample of clean disk maser galaxies are needed to verify the result. In addition, higher-resolution than the $7\farcs4$ for *WISE* band 3 are needed to eliminate contamination from star formation and stars in the host galaxy and verify the correlation.

5. CONCLUSIONS

We present high-resolution VLBI observations of five new maser systems: J0437+2456, ESO 558–G009, NGC 5495, Mrk 1029 and NGC 1320. The maser systems in J0437+2456, ESO 558–G009 and NGC 5495 clearly delineate edge-on maser disks and we measure their central black hole masses by fitting a Keplerian curve to their rotation profiles. The best-fit SMBH mass results are $(2.9 \pm 0.3) \times 10^6\,M_\odot$ for J0437+2456, $(1.7 \pm 0.1) \times 10^7\,M_\odot$ for ESO 558–G009, and $(1.1 \pm 0.2) \times 10^7\,M_\odot$ for NGC 5495.

The maser spectrum in Mrk 1029 does not show a typical disk maser configuration, though the VLBI data could be fitted by the disk model, from which we get the SMBH mass of $(1.64 \pm 0.45) \times 10^6\,M_\odot$. Future VLBI observations that detect maser features at higher rotation velocities could confirm the disk model. For NGC 1320, the maser distribution presents a more complicated picture. Some of the maser spots may trace outflowing gas while others may come from a disk. Our data do not provide a robust black hole mass in this case. The preliminary SMBH mass under the Keplerian disk model is $(5.3 \pm 0.4) \times 10^6\,M_\odot$.

With these new measurements, we define a new sample of VLBI-confirmed "clean" maser disks and we use this sample to investigate relationships between maser disk size, black hole mass, and AGN luminosity. Relating maser disk radii to the SMBH mass, our new measurements together with other works confirm the empirical upper envelope of $R_{\rm out} \propto 0.3 M_{\rm SMBH}$ reported in Wardle & Yusef-Zadeh (2012). We use currently available X-ray 2–10 keV measurements, [O III] measurements, and *WISE* 10 μm measurements as indicators for the AGN luminosity for the disk maser sample and identify a possible correlation between maser disk outer radii and *WISE* luminosity with a high Spearman's rank coefficient of 0.8. We do not see similar correlations with X-ray 2–10 keV

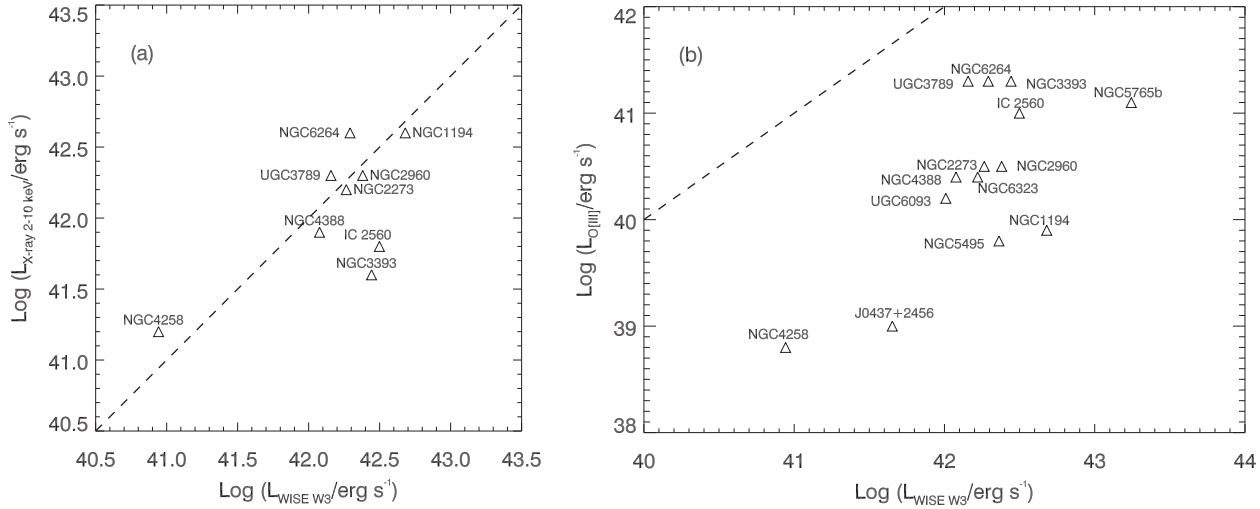

Figure 8. Comparison between the *WISE* Band 3 luminosity with (a) the X-ray 2–10 keV luminosity and (b) the [O III] luminosity. The dashed line shows where the two luminosities are equal, in both plots. The *WISE* Band 3 luminosities come from our measurement of the central pixel value, [O III] data come from Greene et al. (2010) and SDSS online listings, and X-ray 2–10 keV results all come from Castangia et al. (2013). We list the *WISE* luminosity and [O III] luminosity in Table 5.

luminosity or [O III] luminosity data. If confirmed, this correlation suggests that the outer radius of maser disks is determined by the molecular gas kinetic temperature approaching $T_{\rm min} \approx 400$ K, which is essential for pumping water masers.

FG gratefully acknowledges support provided by the National Radio Astronomy Observatory (NRAO) through the Grote Reber Doctoral Fellowship, and support in part by the Major Program of National Natural Science Foundation of China (grants 11590780 and 11590784) and the Strategic Priority Research Program The Emergence of Cosmological Structures of the Chinese Academy of Sciences, grant No. XDB09000000. The National Radio Astronomy Observatory is a facility of the National Science Foundation operated under cooperative agreement by Associated Universities, Inc. This research has made use of the NASA/IPAC Extragalactic Database (NED), which is operated by the Jet Propulsion Laboratory, California Institute of Technology, under contract with the National Aeronautics and Space Administration.

Facilities: VLBA, VLA, GBT, Effelsberg.

APPENDIX
$L(R_{\rm out})$ FOR WATER MASERS

If the outer radius $R_{\rm out}$ of a circumnuclear water maser disk is set by the requirement that the kinetic temperature is at least $T_{\rm min}$, then the inverse-square law suggests it varies with AGN luminosity L as $R_{\rm out} \propto L^{1/2}$ in radiative equilibrium. The upper energy level of the 6_{16}–5_{23} 22 GHz water transition, expressed as a temperature, is $E_u/k \approx 640$ K, so 22 GHz water masers must originate in molecules with kinetic temperatures approaching 640 K. The minimum kinetic temperature is $T_{\rm min} \approx 400$ K (Neufeld et al. 1994).

The water molecules are mixed with dust, and the dust temperature T_d is determined by the local radiation energy density $u_{\rm rad}$. From Equations (24.19) and (24.20) in Draine (2011),

$$T_d \approx 20\, U^{1/6} \tag{6}$$

where the radiation parameter U is defined by

$$U \equiv \frac{u_{\rm rad}}{u_\star} \tag{7}$$

and $u_\star \approx 1.05 \times 10^{-12}$ erg cm^{-3} is the interstellar radiation energy density in the Solar neighborhood. Thus in CGS units

$$T_d \approx 2000\, u_{\rm rad}^{1/6}. \tag{8}$$

At a distance $R_{\rm out}$ from an isotropic point source of total luminosity L,

$$u_{\rm rad} = \frac{L}{4\pi R_{\rm out}^2 c} \tag{9}$$

so

$$R_{\rm out} \approx \left(\frac{2000}{T_{\rm min}}\right)^3 (4\pi c)^{-1/2} L^{1/2}. \tag{10}$$

In astronomically convenient units,

$$\left(\frac{R_{\rm out}}{\rm pc}\right) \approx \left(\frac{L}{2.3 \times 10^{44}\ {\rm erg\ s^{-1}}}\right)^{1/2} \left(\frac{400\ {\rm K}}{T_{\rm min}}\right)^3 \tag{11}$$

or

$$\log\left(\frac{R_{\rm out}}{\rm pc}\right) \approx 0.5\,[\log(L) - 44.36] - 3\log\left(\frac{T_{\rm min}}{400\ {\rm K}}\right) \tag{12}$$

Inserting $L = 2.3 \times 10^{44}$ erg s^{-1} and $R_{\rm out} = 1$ pc $\approx 3.09 \times 10^{18}$ cm into Equation (9) gives $u_{\rm rad} \sim 10^{-4}$ erg cm^{-3} and $U \sim 10^8$.

REFERENCES

Braatz, J. A., & Gugliucci, N. E. 2008, ApJ, 678, 96
Braatz, J. A., Henkel, C., Greenhill, L. J., Moran, J. M., & Wilson, A. S. 2004, ApJL, 617, 29
Braatz, J. A., Reid, M. J., Humphreys, E. M. L., et al. 2010, ApJ, 718, 657
Braatz, J. A., Wilson, A. S., & Henkel, C. 1996, ApJS, 106, 51
Braatz, J. A., Wilson, A. S., & Henkel, C. 1997, ApJS, 110, 321
Castangia, P., Panessa, F., Henkel, C., Kadler, M., & Tarchi, A. 2013, MNRAS, 436, 3388
Collison, A. J., & Watson, W. D. 1995, ApJL, 452, L103
Constantin, A. 2012, JPhCS, 372, 012047

Deller, A. T., Tingay, S. J., Bailes, M., & West, C. 2007, PASP, 119, 318
de Vaucouleurs, G., de Vaucouleurs, A., Corwin JR., H. G., et al. 1991, Third Reference Catalogue of Bright Galaxies, Version 3.9 (New York: Springer)
Draine, B. T. 2011, Physics of the Interstellar and Intergalactic Medium (Princeton, NJ: Princeton Univ. Press)
Draine, B. T., & Li, A. 2007, ApJ, 657, 810
Fu, H., Yan, L., Scoville, N. Z., et al. 2010, ApJ, 722, 653
Gammie, C. F., Narayan, R., & Blandford, R. 1999, ApJ, 516, 177
Gao, F., Braatz, J. A., Reid, M. J., et al. 2016, ApJ, 817, 128
Greene, J. E., Peng, C. Y., Kim, M., et al. 2010, ApJ, 721, 26
Greene, J. E., Seth, A., Kim, M., et al. 2016, ApJL, 826, L32
Greenhill, L. J., Booth, R. S., Ellingsen, S. P., et al. 2003, ApJ, 590, 162
Greenhill, L. J., & Gwinn, C. R. 1997, Ap&SS, 248, 261
Greenhill, L. J., Jiang, D. R., Moran, J. M., et al. 1995, ApJ, 440, 619
Greenhill, L. J., Kondratko, P. T., Moran, J. M., & Tilak, A. 2009, ApJ, 707, 787
Herrnstein, J. R., Moran, J. M., Greenhill, L. J., Trotter, A. S., et al. 1999, Nature, 400, 539
Heckman, T. M., Kauffmann, G., Brinchmann, J., et al. 2004, ApJ, 613, 109
Herrnstein, J. R., Moran, J. M., Greenhill, L. J., & Trotter, A. S. 2005, ApJ, 629, 719
Ho, L. C., Filippenk, A. V., & Sargent, W. L. W. 1997, ApJS, 112, 315
Huchra, J. P., Vogeley, M. S., & Geller, M. J. 1999, ApJS, 121, 287
Humphreys, E. M. L., Reid, M. J., Greenhill, L. J., Moran, J. M., & Argon, A. L. 2008, ApJ, 672, 800
Humphreys, E. M. L., Reid, M. J., Moran, J. M., Greenhill, L. J., & Argon, A. L. 2013, ApJ, 775, 13
Ishihara, Y., Nakai, N., Iyomoto, N., et al. 2001, PASJ, 53, 215
Kondratko, P. T., Greenhill, L. J., & Moran, J. M. 2005, ApJ, 618, 618
Kondratko, P. T., Greenhill, L. J., Moran, J. M., et al. 2006, ApJ, 638, 100
Kondratko, P. T., Greenhill, L. J., Moran, J. M., et al. 2008, ApJ, 678, 87
Kormendy, J., & Ho, L. C. 2013, ARA&A, 51, 511
Kuo, C. Y., Braatz, J. A., Condon, J. J., et al. 2011, ApJ, 727, 20
Liu, X., Zakamska, N. L., Greene, J. E., et al. 2009, ApJ, 702, 1098
Mamyoda, K., Nakai, N., Yamauchi, A., Diamond, P., & Hure, J. 2009, PASJ, 61, 1143
Masini, A., Comastri, A., Balokovic, M., et al. 2016, A&A, 589, 59
Masters, K. L., Springob, C. M., Haynes, M. P., & Giovanelli, R. 2006, ApJ, 653, 861
Mateos, S., Alonso-Herrero, A., Carrera, F. J., et al. 2012, MNRAS, 426, 3271
McConnell, N. J., & Ma, C-P. 2013, ApJ, 764, 184
Mioduszewski, A., & Kogan, L. 2000, AIPS Memo, 110
Miyoshi, M., Moran, J. M., Herrnstein, J. R., et al. 1995, Natur, 373, 127
Neufeld, D. A., & Maloney, P. R 1995, ApJL, 447, L17
Neufeld, D. A., Maloney, P. R., & Conger, S. 1994, ApJL, 436, L127
Pesce, D. W., Braatz, J. A., Condon, J. J., et al. 2015, ApJ, 810, 65
Planck Collaboration, Ade, P. A. R., Aghanim, N., et al. 2016, A&A, 594, 13
Reid, M. J., Braatz, J. A., Condon, J. J., et al. 2009, ApJ, 695, 287
Reid, M. J., Braatz, J. A., Condon, J. J., et al. 2013, ApJ, 767, 154
Reid, M. J., Menten, K. M., Brunthaler, A., et al. 2014, ApJ, 783, 130
Riess, A. G., Macri, L. M., Hoffmann, S. L., et al. 2016, ApJ, 826, 56
Shakura, N. I., & Sunyaev, R. A. 1973, A&A, 24, 337
Stern, D., Assef, R. J., Benford, D. J., et al. 2012, ApJ, 753, 30
Thompson, A. R., Moran, J. M., & Swenson, G. W., Jr. 2001, Interferometry and Synthesis in Radio Astronomy (New York: Wiley)
van den Bosch, R. C. E., Greene, J. E., Braatz, J. A., Constantin, A., & Kuo, C. Y. 2016, ApJ, 819, 11
Wardle, M., & Yusef-Zadeh, F. 2012, ApJL, 750, L38
Wright, E. L., Eisenhardt, P. R. M., Mainzer, A. K., et al. 2010, AJ, 140, 1868
Yan, L., Donoso, E., Tsai, C-W., et al. 2013, ApJ, 145, 55
Zakamska, N. L., Strauss, M. A., Krolik, J. H., et al. 2003, AJ, 126, 2125
Zhang, J. S., Henkel, C., Kadler, M., et al. 2006, A&A, 450, 933
Zhang, J. S., Henkel, C., Guo, Q., Wang, H. G., & Fan, J. H. 2010, ApJ, 708, 1528
Zhang, J. S., Henkel, C., Guo, Q., & Wang, J. 2012, A&A, 538, 152
Zhu, G., Zaw, I., Blanton, M. R., & Greenhill, L. J. 2011, ApJ, 742, 73